applied sciences

MDPI

Article

Supporting Imaging of Austenitic Welds with Finite Element Welding Simulation—Which Parameters Matter?

Michał K. Kalkowski [1,2,*], Zoltán Bézi [3,*], Michael J. S. Lowe [2], Andreas Schumm [4], Bernadett Spisák [3,*] and Szabolcs Szavai [3]

1 Institute of Sound and Vibration Research, University of Southampton, Southampton SO17 1BJ, UK
2 Mechanical Engineering, Imperial College London, London SW7 2AZ, UK; m.lowe@imperial.ac.uk
3 Engineering Division, Bay Zoltán Nonprofit Ltd. for Applied Research, Iglói Street 2, 3519 Miskolc, Hungary; szabolcs.szavai@bayzoltan.hu
4 EDF Labs Les Renardières, EDF R&D, Avenue des Renardières, 77818 Moret sur Loing, France; andreas.schumm@edf.fr
* Correspondence: m.kalkowski@soton.ac.uk (M.K.K.); zoltan.bezi@bayzoltan.hu (Z.B.); bernadett.spisak@bayzoltan.hu (B.S.)

Abstract: The basic principle of ultrasound is to relate the time of flight of a received echo to the location of a reflector, assuming a known and constant velocity of sound. This assumption breaks down in austenitic welds, in which a microstructure with large oriented austenitic grains induces local velocity differences resulting in deviations of the ultrasonic beam. The inspection problem is further complicated by scattering at grain boundaries, which introduces structural noise and attenuation. Embedding material information into imaging algorithms usually improves image quality and aids interpretation. Imaging algorithms can take the weld structure into account if it is known. The usual way to obtain such information is by metallurgical analysis of slices of a representative mock-up fabricated using the same materials and welding procedures as in the actual component. A non-destructive alternative to predict the weld structure is based on the record of the welding procedure, using either phenomenological models or the finite element method. The latter requires detailed modelling of the welding process to capture the weld pool and the microstructure formation. Several parameters are at play, and uncertainties intrinsically affect the process owing to the limited information available. This paper reports a case study aiming to determine the most critical parameters and levels of complexity of the weld formation models from the perspective of ultrasonic imaging. By combining state-of-the-art welding simulation with time-domain finite element prediction of ultrasound in complex welds, we assess the impact of the modelling choices on the offset and spatial spreading of defect signatures. The novelty of this work is in linking welding simulation with ultrasonic imaging and quantifying the effect of the common assumptions in solidification modelling from the non-destructive examination perspective. Both aspects have not been explored in the literature to date since solidification modelling has not been used to support ultrasonic inspection extensively. The results suggest that capturing electrode tilt, welding power, and weld path correctly is less significant. Bead shape was identified as having the greatest influence on delay laws used to compute ultrasonic images. Most importantly, we show that neglecting mechanical deformation in FE, allowing for simpler thermal simulation supplemented with a phenomenological grain growth loop, does not reduce the quality of the images considerably. Our results offer a pragmatic balance between the complexity of the model and the quality of ultrasonic images and suggest a perspective on how weld formation modelling may serve inspections and guide pragmatic implementation.

Keywords: austenitic welds; ultrasonic imaging; total focusing method; delay laws; weld formation; welding simulation; solidification; non-destructive evaluation (NDE); weld inspection; ultrasonic testing

Citation: Kalkowski, M.K.; Bézi, Z.; Lowe, M.J.S.; Schumm, A.; Spisák, B.; Szavai, S. Supporting Imaging of Austenitic Welds with Finite Element Welding Simulation—Which Parameters Matter? *Appl. Sci.* **2023**, *13*, 7448. https://doi.org/10.3390/app13137448

Academic Editor: Guijun Bi

Received: 25 April 2023
Revised: 16 June 2023
Accepted: 20 June 2023
Published: 23 June 2023

1. Introduction

Ultrasonic imaging of full matrix capture acquisitions using TFM (total focusing method [1]) or derived algorithms typically rely on the assumption that ultrasound propagates with constant (and usually isotropic) velocity within the part to be inspected. This assumption greatly simplifies the calculation of shortest travel times between a transmitting element and an observation point, which needs to be performed $N_{\text{elements}} \times N_{\text{observation point}}$ times for typical reconstruction algorithms.

However, the assumption of constant travel time breaks down within austenitic welds [2], in which a microstructure with large oriented austenitic grains causes local velocity differences, which affect the ultrasonic beam; it suffers from multiple deviations at grain boundaries, and sometimes is split into several beams, modifying the focusing properties significantly. If reconstructed ignoring the actual microstructure, the resulting image will inevitably fail to predict the correct defect location [3,4]. Embedding material information into imaging algorithms involves calculating delay laws for the imaged domain, accounting for heterogeneous anisotropy [5]. Material information required for such calculations can be obtained from several sources, including the destructive examination (Electron Backscatter Diffraction—EBSD, metallography), ultrasonic inversion (within the ADVISE project, we have developed several techniques for determining the weld structure [6–8]), or weld formation simulation. This paper addresses the last mentioned approach, analysing the impact of a few weld formation model parameters from the ultrasonic imaging perspective.

Thick austenitic welds are characterised by long columnar grains with locally preferential orientations. To model ultrasound propagation, one can either develop a model based directly on the measured microstructure (grain-scale) or use its homogenised counterpart [9]. It is common in the non-destructive evaluation (NDE) community to homogenise grains with similar orientations and create a macroscale description, replacing clusters of grains with a locally homogeneous anisotropic material (transversely isotropic) rotated according to the dominant orientations of grains. Such a description typically takes the form of a regular map, splitting the domain into square-shaped regions for which homogenised dominant orientation is specified. For most practical cases, a homogenisation scale of 2 mm is considered sufficient [9,10].

The grain layout described above is responsible for two detrimental effects on imaging, beam deviation, and increased noise. Since the orientation of grains varies across the weld, the ultrasound no longer travels along straight paths. The complex, curved ray paths lead to misinterpretation of conventional inspections in which the position of the reflectors cannot be judged reliably any more. For imaging, where isotropic delay laws are traditionally assumed, defect signatures can be misplaced. The other effect, which is often dominant, is the reduction in the signal-to-noise ratio; as with unmatched delay laws, the TFM's beamforming is out of focus and spreads the energy of the scatterer across the surrounding area. Further complicated by grain noise, which is always present in coarse grain materials, the reduction in the signal-to-noise ratio (SNR) may bury the signature of interest below the noise floor. These two effects can be tackled by embedding material information into imaging. One way to do this is to precompute delay laws assuming a given grain orientation map for the weld under test and use these delay laws in TFM imaging.

The first attempts to describe grain orientations used simple geometric representations, for instance, the single-angle symmetric arrangement in [11], or the multi-layer model [12]. The first flexible gold-standard model—the Ogilvy map—was proposed a few years earlier [13] and allowed for a continuous orientation variation to be modelled. These descriptions originated from the observations of metallography images and did not link to any physical parameters and intuitions about the welding process. Currently, the most commonly used model is MINA [9], which predicts the orientations based on the information from the welder's notebook. Representing the weld deposition process phenomenologically provided a mathematically simple framework with parameters directly

linked to weld manufacturing. However, MINA has its limitations, both with regard to welding methods it can cover and allowable weld complexity.

The literature offers several approaches to modelling weld microstructures numerically, considering specific simplifying assumptions about grain geometry or orientation [14–18]. The finite element analysis (FEA) is suitable for solving various problems in solid mechanics, heat transport and other physical domains. However, FEA is primarily a continuum technique and, until recently, had limited uptake for simulating the microstructural mass transfer and evolution, both inherent in the welding process. Finite element modelling of welding encapsulates rather complex phenomena and involves considerable effort. On the other hand, the intuition is that only a portion of the information provided by such models is used in imaging. For instance, solidification simulations often focus on predicting residual stress in welds, an aspect of little benefit for supporting ultrasonic imaging. Further, such an FE model often requires numerous input parameters (bead shapes, location, source power, material properties and composition, etc.) and only a fraction of this can be recovered from the manufacturing procedure. A significant proportion needs to be inferred, calculated based on some assumptions or assumed based on limited detailed studies available. This manuscript reports on a case study shedding light on the much-desired pragmatic balance between the simulation cost and its accuracy when employed as a supporting tool for ultrasonic imaging. The aim of the paper is to assess different levels of complexity of the numerical weld formation model. We use a case study of a V-weld austenitic weld which was manufactured for the ADVISE project. However, the present study focuses on the impact of weld formation model parameters on corrected delay laws for imaging and hence, uses only numerical simulations to better expose the effect of the considered configurations.

To the authors' knowledge, finite element modelling of welding has not been extensively used to support ultrasonic imaging. Computational cost and complexity are the main reasons for preferring simple descriptions; however, the versatility of finite elements enables the capturing of a broader range of configurations, geometries, welding methods, and contexts. This paper reports on the development of a simplified finite element procedure, considerably reducing the calculation time. With this tool, we performed a parametric study analysing the effect of several weld formation model parameters on imaging. We consider a specific use case—an austenitic stainless steel mock-up manufactured during this research. While this is an isolated example, the insight we offer will hopefully provide a better understanding of the importance of weld formation model parameters and guide further research on this topic. To our knowledge, this is the first comprehensive study devoted to the use of finite element welding simulation in supporting ultrasonic inspection. We adopt an ultrasonic imaging perspective and evaluate the effect of the welding simulation parameters by analysing TFM images computed using the delay laws based on weld formation simulation. This approach focuses on the end-user and generates insights directly relevant to the NDE community, striking a pragmatic balance between the approximations in welding simulation and the requirements of imaging algorithms. We show that coupled thermo-mechanical simulation is not necessary to deliver material information suitable for imaging. Instead, we propose a computationally cheaper procedure, which uses thermal-only finite element simulation and a phenomenological grain growth loop in post-processing. This approach offers significant computational gains while—as we show—producing results relevant to ultrasonic non-destructive testing. Together with the identification of parameters with the strongest influence, our results pave the way towards including welding simulation in NDE workflows.

2. Estimation of the Welding Parameters

It is well known that the shape and temperature distribution of the weld pool depend on the type of welding process, the welding parameters (welding speed, wire diameter, wire feed rate, tension, current density, workpiece inclination, etc.) and the welding materials (heat transfer, specific heat, latent heat); therefore, a systematic sensitivity analysis has been performed to identify the critical parameters that are required to predict the most realistic

grain orientation distribution. The first step of a welding simulation is the definition of the welding parameters, which are essential for numerical analysis. For this purpose, a welding specimen was prepared. This study is based on a V-weld manufactured for the ADVISE project at the University of Stuttgart (MPA). It was an originally circumferential weld joining two 39 mm thick pipes, which was then sectioned and used for ultrasonic evaluation and examination. The pipes with a nominal outside diameter of 517 mm and made of 1.4550 steel were joined using ESAB OK 61.30 filler material and manual shielded metal arc welding (SMAW) technique. Figure 1 shows the resulting weld seam and sectioning. The threads were laid out from right to left, and their arrangement and the metallographic image after sectioning are shown in Figure 2. For experimental convenience, the curved surfaces of several sections were flattened, and this modification has been adopted in the present study. The chemical compositions of the materials are listed in Table 1. Using these data, the temperature-dependent material properties were derived using the JMatPro software [19–21]. These properties include Young's modulus (E), yield strength (σ_y), specific heat capacity (c), thermal expansion coefficient (α), and thermal conductivity (λ). The thermo-mechanical properties at 20 °C are listed in Table 2.

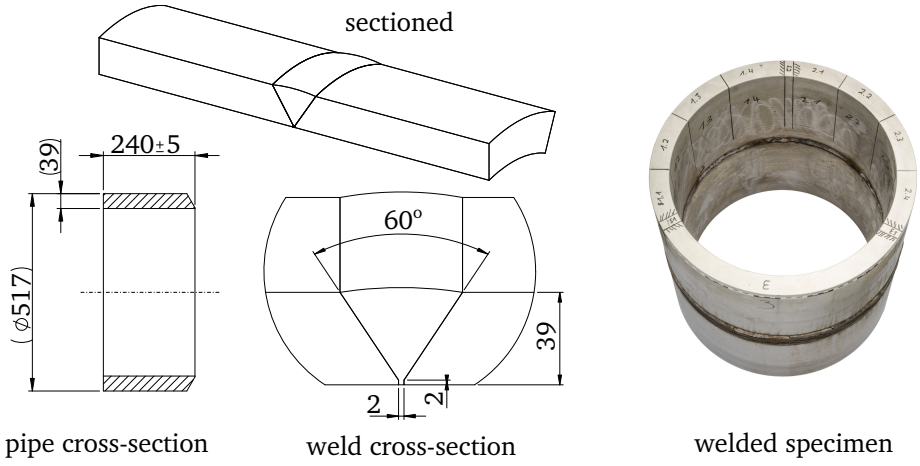

Figure 1. Schematic diagram and a photograph of the considered sample.

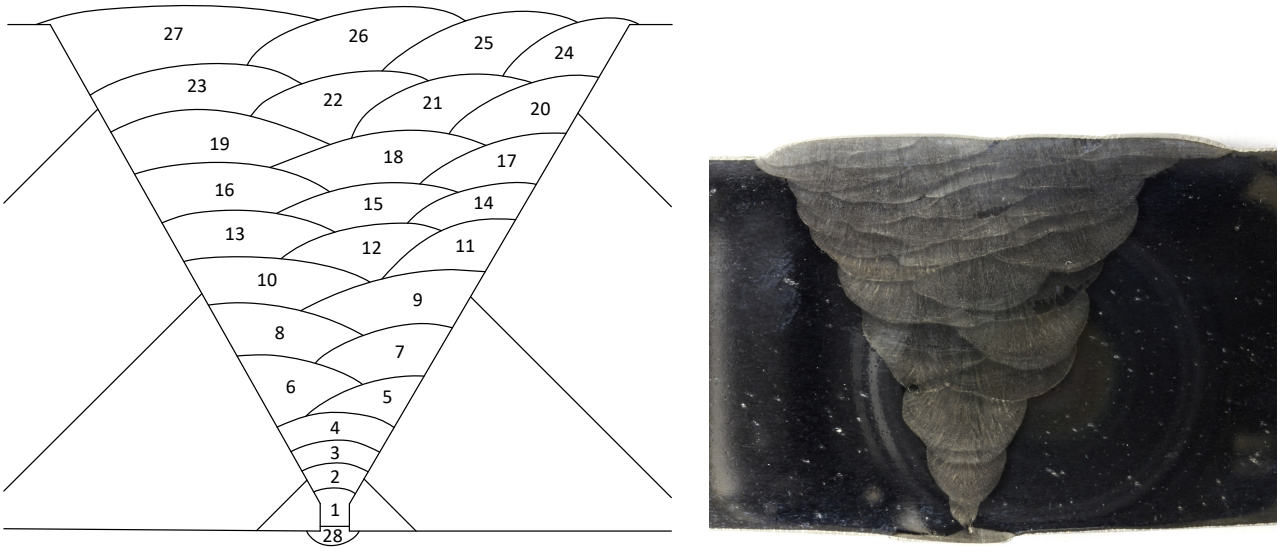

(**a**) Layout of passes (**b**) Metallography

Figure 2. Layout of passes from the welder's notebook and metallography image.

Table 1. Chemical composition.

Material	C%	Si%	Mn%	P%	S%	Cr%	Ni%	Mo%	Cu%	N%	Nb%
1.4550 steel	<0.08	<1.00	<2.00	<0.045	<0.03	17.00–19.00	9.00–12.00	-	-	-	1.00
ESAB OK 61.30	<0.030	0.50–1.00	0.50–1.20	<0.025	<0.020	18.5–20.5	9.0–11.0	<0.5	<0.5	<0.15	-

Table 2. Thermo-mechanical properties at 20 °C .

Material Name	E (GPa)	σ_y (MPa)	c (J/kg°C)	α (10^{-5}/°C)	λ (W/m°C)
1.4550 steel	195.62	17.88	204.69	449.48	14.46
ESAB	199.62	17.25	221.03	450.29	14.89

According to the received welding report, it is composed of 12 layers with different numbers of welds on each layer:

- layers 1–4: one pass;
- layers 5–7: two passes;
- layers 8–10: three passes;
- layers 11–12: four passes;
- layers 13: back weld.

The welding consists of a total of 28 weld passes, where the first is the root pass, the 2nd to 23rd are the filler passes, the 24th to 27th are the cover passes, and, finally, the 28th is the back weld.

The detailed welding report is shown in Table 3; it includes the welding position, the fillers, and a few welding parameters. Unfortunately, these are insufficient for developing welding simulations, and determining other parameters is necessary. The desired parameters include the nugget areas, the welding velocity and the welding power; the following sections outline the origin of the finally adopted values.

Table 3. The welding report.

Number of Layers	Welding Process	Welding Position	Filler Material	Electrode Diameter (mm)	Current Type and Polarity	Current (A)	Electrode Run-Out Length (mm)	Burn-Off Time (s)	Electrode Inclination (°)
1	141	PA *	EAS 2-IG	2.4	DC negative	120	40–60	60	60–80
2	111	PA	ESAB OK 61.30	4.0	DC positive	140	130	60	60–80
3–9	111	PA	ESAB OK 61.30	5.0	DC positive	180	160	65	60–80
10–12	111	PA	ESAB OK 61.30	4.0	DC positive	150	125	60	60–80
13	111	PA	ESAB OK 61.30	4.0	DC positive	150	150	60	80

* Flat position.

2.1. Size of the Nugget Areas

There are two ways to calculate the missing welding parameters, the first is to estimate them according to the standard, and the second is to calculate the welding parameters from the welding report. Two procedures were used for welding the specimen, gas tungsten arc welding (GTAW) and SMAW. Based on reference [22], the following equations can be used to calculate the voltage. For GTAW with currents I up to 600 A, the voltage U is

$$U = 13 + 0.012I, \quad (1)$$

It should also be noted that the welding speed must be less than $v = 4$ mm/s and the process efficiency $\eta = 0.6$. The SMAW voltage is calculated using the following equation:

$$U = 20 + 0.04. \quad (2)$$

Here the maximum welding speed is the same as in the case of GTAW, but the efficiency is higher, $\eta = 0.8$. From this, the welding heat input can be calculated using the following equation:

$$P = \eta UI/v. \quad (3)$$

The next step is calculating the nugget areas, which can be determined from the rate of the welded volume and the electrode run-out length. The volume can be calculated from the electrode's length and diameter. Two types were used for the studied weld, the EAS 2-IG and the ESAB OK 61.30. The length of the ESAB OK 61.30 electrode is 350 mm, but it is safe to estimate that 50 mm of that length is not consumed in the welding process. From the data provided, the estimated values of stress, volume, and void area were determined and are shown in Table 4.

Table 4. Estimated nugget areas based on the size of the electrode.

Filler Material	Current (A)	Voltage (V)	Welding Heat Input (kJ/mm)	Electrode Diameter (mm)	Electrode Length (mm)	Electrode Run-Out Length (mm)	Volume (mm^3)	Real Nugget Area (mm^2)
EAS 2-IG	120	14.4	0.2599	2.4	-	50	-	- *
ESAB OK 61.30	140	25.6	0.7168	4.0	300	130	3769.91	28.999
ESAB OK 61.30	150	26.0	0.7800	4.0	300	125	3769.91	30.159
ESAB OK 61.30	150	26.0	0.7800	4.0	300	150	3769.91	25.133
ESAB OK 61.30	180	27.2	0.9792	5.0	300	160	5890.47	36.816

* Determined from full welded area.

The second calculation version of the welding parameters is based on the welding report. The welding speed can be calculated using the given electrode run-out length and burn-off time; the welding heat input can be determined as well. The relationship between the cross-sectional area of the weld filler metal introduced per pass and the electrical heat input per unit length was measured in reference [23] for SMAW welding of austenitic steels. Based on the data in [23], the weld heat input and the area of the nuggets can be estimated for different current values. These values are summarised in Table 5. It should be noted that the equation given in reference [23] does not consider the welding efficiency; therefore, the last column of the table shows the actual nugget areas.

From Tables 4 and 5, it can be seen that with the two methods of calculation, there is a difference of around 20% between the values of the nugget areas. However, comparisons of the final microstructures revealed that this difference had no significant impact. Both methods are therefore applicable.

2.2. Parameters of Welding Spots

In welding simulations, the size of the welding spot has a large influence on the final results. The most widely used mathematical model was developed by J. Goldak et al. [24], where the welding heat sources are based on the Gaussian distribution of power density in space. The first concept of welding simulations was to use an elliptical heat source, but the results were inconsistent with the experimental results. The temperature gradient in front of the heat source was not as steep as expected. Therefore, a combination of two

ellipsoidal heat sources was proposed. The geometric parameters and the Gaussian volume distribution are shown in Figure 3.

Table 5. Calculated nugget areas based on the welding report.

Filler Material	Electrode Run-Out Length (mm)	Burn-Off Time (s)	Welding Speed (mm/s)	Welding Heat Input (kJ/mm)	Nugget Area Based on Ref. [23] (mm^2)	Real Nugget Area (mm^2)
EAS 2-IG	50	60	0.83	1.248	18.714	31.190
ESAB OK 61.30	130	60	2.17	1.323	19.850	24.812
ESAB OK 61.30	125	60	2.08	1.498	22.464	28.080
ESAB OK 61.30	150	60	2.50	1.248	18.720	23.400
ESAB OK 61.30	160	60	2.46	1.591	23.868	29.835

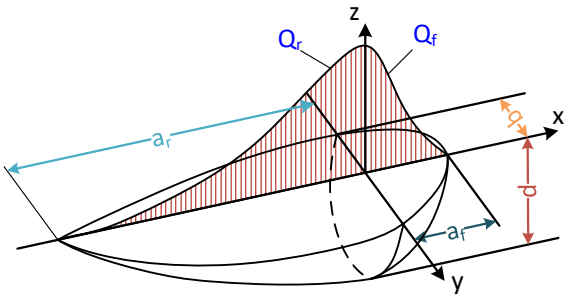

Figure 3. Goldak's double ellipsoid heat source shape.

The power density distribution for the front quadrant can be expressed by the following Equation [24]:

$$q(x,y,z,t) = \frac{6\sqrt{3}f_f Q}{ba_f d\pi\sqrt{\pi}} e^{(-3x^2/b^2)} e^{(-3y^2/d^2)} e^{(-3[z+v(\tau-t)]^2/a_f^2)} \quad (4)$$

In the case of the rear quadrant, a similar equation can be used for the calculation of the power density distribution:

$$(x,y,z,t) = \frac{6\sqrt{3}f_r Q}{ba_r d\pi\sqrt{\pi}} e^{(-3x^2/b^2)} e^{(-3y^2/d^2)} e^{(-3[z+v(\tau-t)]^2/a_r^2)} \quad (5)$$

where f_f is the fraction of the heat deposited in the front quadrant, f_r is the fraction of the heat deposited in the rear quadrant, Q energy input rate (W), τ lag factor for defining the position of the source at time $t = 0$, v is the welding speed (m/s), a_f is the front length of the heat source, a_r is the rear length of the heat source, b is the width of the heat source, d is the depth of the heat source. The equations are written in a fixed (x, y, z) coordinate system. The transformation between the fixed and moving coordinate systems is $\zeta = z+$ vs. $(\tau - t)$. From these equations, it is apparent that to simulate the weld, the front length, rear length, width, and depth of the heat source must be determined. The depth and the width can be identified from a micrograph, while the other values can be estimated with the equations $a_f = 0.6b$ and $a_r = 2.0 \ldots 2.5b$. If the first estimation is based on a construction plan, the so-called design throat (a) can be used to estimate the other geometric parameters. In this case, the depth and width of the heat source can be given by the simple equation $d = a_r + 2.0 \ldots 5.0$ mm and $b = a_r + 1 \ldots 2$ mm.

3. Finite Element Setup

The preceding section determined the welding parameters. As already mentioned, the unknown thermal and mechanical material parameters were obtained using the JMatPro software based on the chemical composition of the materials. This section outlines the development of the finite element welding simulation.

The finite element mesh was built using 2D axisymmetric four-noded solid elements. For the heat flow calculations, thermal boundary conditions were defined. The initial temperature of the nodes (room temperature or interpass temperature) was determined before the first loading step of the thermo-mechanical/thermal analysis. The nodal temperature of weld passes not yet deposited was prescribed in the first step of the calculation to avoid ill-conditioned matrices. A combined temperature-dependent heat transfer coefficient was used in the simulation to model the effects of convection and radiation into the environment. The film coefficient was taken as 20 $Wm^{-2}K^{-1}$, while the radiation coefficient was assumed to be a temperature-independent value of 0.8. As mentioned before, a double-ellipsoidal heat source model was used. Heat generation induced by moving volumetric heat sources was defined as the force load on the element body during the transient thermo-mechanical analysis.

3.1. Simplified Welding Simulation

Full FE simulation of welding is a coupled thermo-mechanical simulation, which includes mechanical deformation and captures grain growth within the FE calculation. Such an approach delivers numerous important outputs, such as residual stresses. In practice, supporting ultrasonic inspection only requires approximate local grain orientations. Moreover, the coupled thermo-mechanical simulation is costly, hindering its implementation in imaging workflows. To address this, this paper proposes a simplified approach in which full FE simulation is used to determine thermal gradients, and a phenomenological loop (analogous to that in MINA [9]) captures grain growth in the post-processing stage. In this approach, the deformation resulting from welding is not taken into account, and grain growth effects are only approximated. Consequently, significant computational savings are possible since the thermal calculations are less time-consuming. In general, the heat source applied during welding produces beads in which the grains grow along the maximum thermal gradient during cooling. This approach is sufficient to determine a realistic grain orientation, ignoring the effect of geometric distortion. Moreover, several welding processes and complex geometries can be investigated using this approach. By neglecting mechanical effects, the computational cost is significantly reduced, allowing large-scale 3D calculations to be implemented. User-specified subroutines were used to implement grain orientation and growth calculation models for the entire welded area. The grain orientation calculation is based on the MINA model, as mentioned above

$$n = 0,\ \alpha_0 = \alpha_{\text{lower box}} \tag{6}$$

$$t_n = \begin{cases} cos(\alpha_{n-1} - \alpha_g), & \text{if } \alpha_{n-1} - \alpha_g < \pi/2 \\ 0, & \text{otherwise} \end{cases} \tag{7}$$

$$\alpha_n = t_n \alpha_{n-1} + (1 - t_n)\alpha_g \tag{8}$$

where α_n is the grain angle, α_g is the direction of the effective temperature gradient, t_n is the parameter representing the change in orientation, and n is the number of iterations used. This parameter n represents the transition between microscopic and macroscopic scales. Unfortunately, the value of n in the FE calculation depends on the cooling rate, so its value is fixed with an equal change in temperature. However, the changes in the temperature gradient are only considered between the beginning and the end of solidification.

3.2. Parameters Studied

The study aimed at determining the relevance of the chosen modelling assumptions and parameters to support the ultrasound inspection. Three types of meshes were generated:

1. Realistic geometry where the back weld and a 2 mm gap with simplified bead shape was considered (Figure 4a);

2. Realistic geometry where the back weld and a 2 mm gap with realistic bead shape was considered, which was built according to the fusion lines of the real weld (Figure 4b);
3. 3D simulation based on Mesh type 1 (Figure 4c).

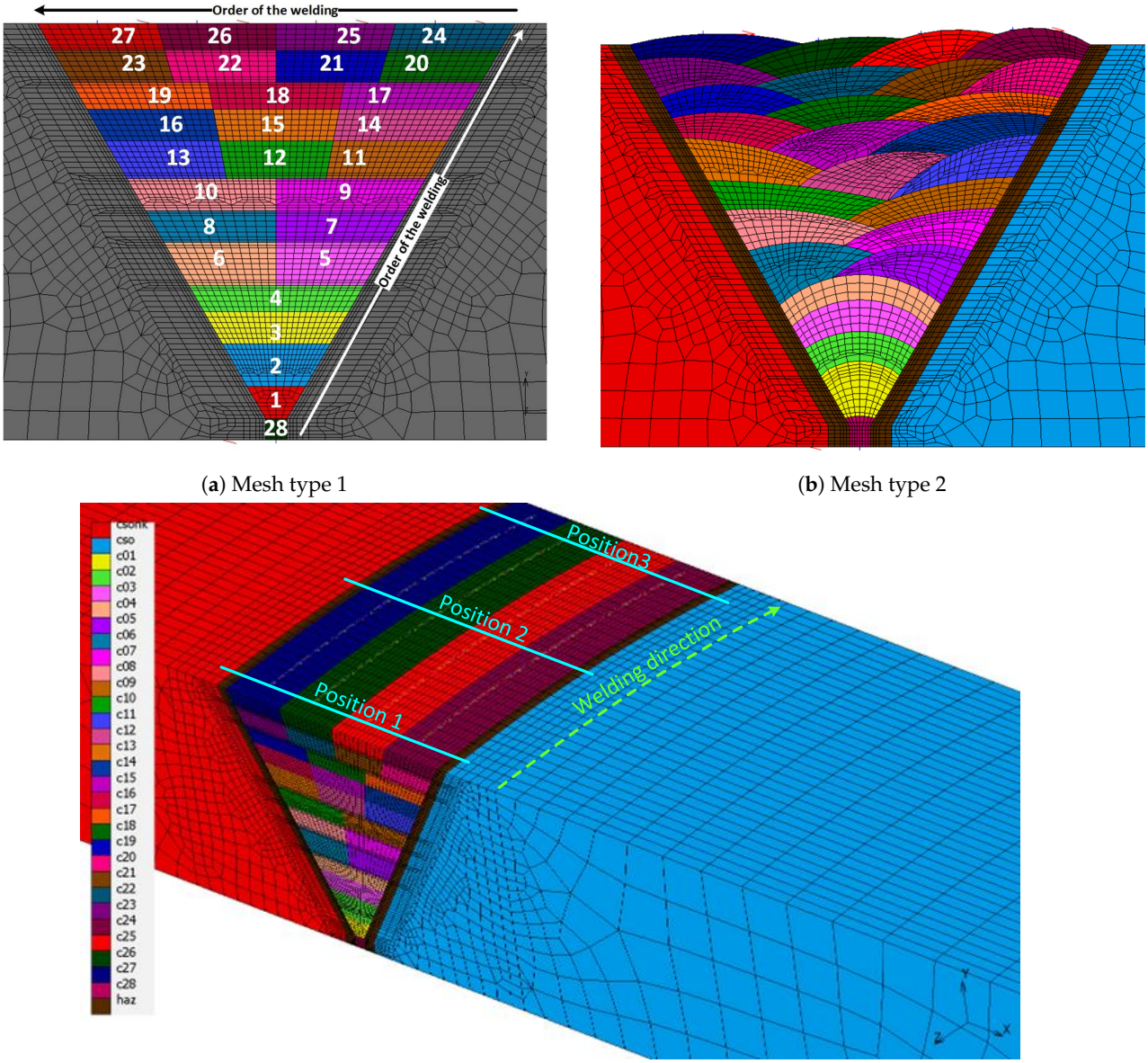

(**a**) Mesh type 1

(**b**) Mesh type 2

(**c**) Mesh type 3

Figure 4. Finite element simulation mesh types.

Table 6 presents all the model variants used in the parametric investigation. Case 1 used simplified weld areas based on the original geometry (mesh 1) and was taken as a reference. The sizes of the cross sections of the beads and the heat sources were determined from the estimated welding parameters (Table 4).

First, we looked at the effect of altering the order of passes. We considered two cases—the continuous sequence from one side to the other (right-to-left in this paper—as in Case 1), and the American layout (Case 2), characterised by interchangeably depositing passes on opposite chamfers (the last pass of a layer is placed in the middle of the weld).

Table 6. Variants considered in the parametric study.

Case	Mesh Type	Simulation Type	Pass Order *	Electrode Tilting	Heat Source	Weld Shape	Welding Heat Input	Position	Weaving Technique
1	1	Thermal	RL	-	Estimated	Simplified	-	-	-
2	1	Thermal	RL (USA)	-	Estimated	Simplified	-	-	-
3	1	Thermal	RL	+8°	Estimated	Simplified	-	-	-
4	1	Thermal	RL	−5°	Estimated	Simplified	-	-	-
5	1	Thermal	RL	-	Estimated	Simplified	+10%	-	-
6	2	Thermal	RL	-	Calculated	Realistic	-	-	Nominal
7	2	Thermal	RL	-	Calculated	Realistic	-	-	Small
8	2	Thermal	RL	-	Calculated	Realistic	-	-	Large
9	3	Thermal	RL	-	Estimated	Simplified	-	Centre	-
10	3	Thermal	RL	-	Estimated	Simplified	-	Arc start	-
11	3	Thermal	RL	-	Estimated	Simplified	-	Arc finish	-
12	1	Thermo-mechanical	RL	-	Estimated	Simplified	-	-	-

* RL—right to left

Next, we analysed the effect of electrode tilt (Case 3 and Case 4). The metallography shown in Figure 2 suggests an electrode tilt for the higher passes. Therefore, from pass 5 to 27, two electrode tilting angles were analysed—+8° (Case 3) and −5° (Case 4). In Case 5, higher welding power was applied, giving a 10% increase in line energy.

The study also included comparing models with realistic weld bead geometries. In Cases 6, 7, and 8 (mesh 2), their shapes followed the fusion lines of the sample. In SMAW welding, the weaving technique was used in the welding process, resulting in the weld beads being arranged in a zigzag pattern. This technique is widespread and enables the formation of wide weld lines. Since an accurate simulation of the weaving movement was challenging, we represented it with multiple heat sources. Figure 5 shows the weaving technique's effects on the pool shape and the temperature gradient orientation, indicating that a larger number of heat sources makes the melted area more shallow and wider. Cases 6, 7, and 8 considered nominal, smaller, and larger bead shapes, respectively.

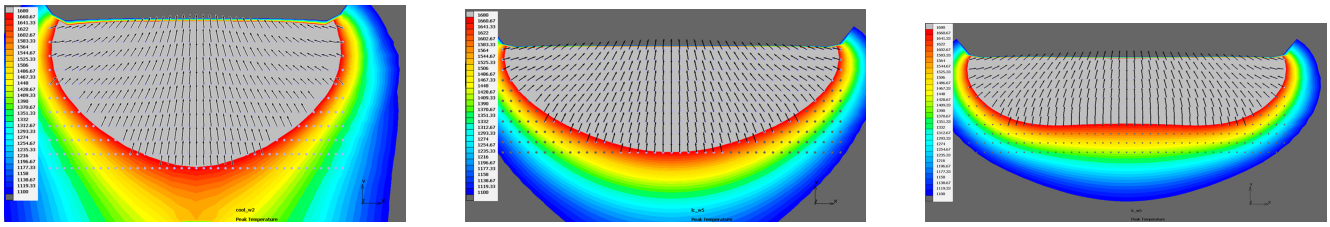

(**a**) No weaving/small weaving (**b**) Nominal weaving with two heat source (**c**) Large weaving with three heat source

Figure 5. Weld pool formation in case of SMAW.

Cases 9, 10, and 11 came from the 3D simulation (mesh 3), which was possible thanks to the simplified grain growth modelling procedure (otherwise, computation time would be impractical). We used full 3D thermal finite element simulation and applied the approximate epitaxial loop on the resulting thermal gradients to obtain the final orientation maps. Figure 4c shows the positions corresponding to the probed locations along the welding direction. Position 1 (Case 10) refers to the starting position of the arc, position 2 illustrates the representative cross-section of the weld (centre—Case 9), and the final position 3 corresponds to the arc finish section (Case 11).

Finally, we assessed the impact of simplifying welding simulation using our proposed workflow. We compared Case 1 against a full, coupled thermo-mechanical (Case 12), which included the mechanical effects.

4. Simulating Array Acquisitions and Array Imaging

Grain orientation maps obtained from weld formation modelling were used in ultrasonic modelling to discover their effect on the images for chosen defect scenarios. Since our interest was to discover the effect of weld model parameters on the images, simulation was seen as the best way to achieve that. If comparing to experimental data, the main questions would be whether the material parameters assumed in simulations reflect those in the real sample, if the geometry was measured accurately, etc. Conversely, modelling allows us to retain control of the configuration and focus solely on the effect of chosen weld model parameter variations.

Ultrasonic images were computed using a classical total focusing method (TFM) approach

$$I(x,y) = \left| \sum_{i=1}^{M} \sum_{j=1}^{M} \left[u_{i,j}\left(\tau_{i\to(x,y)} + \tau_{j\to(x,y)}\right) + \jmath \hat{u}_{i,j}\left(\tau_{i\to(x,y)} + \tau_{j\to(x,y)}\right) \right] \right| \tag{9}$$

where (x, y) is the position in the physical domain, M is the number of elements in the array, $u_{i,j}$ is the response of element i to excitation at element j, $\tau_{i\to(x,y)}$ is the time-of-flight between element i and point (x, y) (called a delay law) and $\hat{u}_{i,j}$ is the Hilbert transform of $u_{i,j}$ [25]. The analytic signal $u_{i,j} + \jmath \hat{u}_{i,j}$ is the output of "Hilbert" functions in major scientific computing environments (e.g., `scipy`, MATLAB).

Two modelling methods contributed to this paper, time-domain finite element simulations were used to model virtual ultrasonic array acquisitions, mimicking the experiments (outputting time traces $u_{i,j}$), while a shortest ray path model was used to calculate delay laws ($\tau_{(x,y)\to i}$). Conventionally, TFM imaging assumes straight ray paths and constant isotropic wave velocity to calculate delay laws. The isotropic assumption often fails dramatically in complex-structured materials, and the present paper shows how weld formation simulations can improve the legibility of the images.

4.1. Finite Element Modelling of Ultrasound

Time-domain finite element simulations of ultrasound were developed and executed in Pogo, a fast GPU-based explicit elastodynamic solver developed at Imperial College London. The use of FE is motivated by its versatility in representing any geometry, material composition, etc., and the ability to represent the rich physics of wave propagation. Modelling ultrasound with FE is a standard technique in NDE, well-documented, verified, and validated in the literature, both against experiments, analytical theories, and (for Pogo) with equivalent commercial solvers, e.g., [26–29], so this step is not reported in this paper. Instead, we follow the agreed guidelines for developing FE models by ensuring that a sufficient number of elements per wavelength is included. The geometry of the weld and the transducer setup remained constant across all simulations; the only differing part was the local orientations. Based on the most common defect types of interest, we chose three defect scenarios for further consideration—(i) three single-drilled-holes (SDHs) along the left chamfer, (ii) three SDHs along the right chamfer, and two notches perpendicular to the backwall, close to the weld root. Figure 6 shows the diagram of the numerical configuration with the dimensions and studied defects and the "nominal" grain orientation set. Note that while the defects are drawn on the same image in Figure 6, they were considered as three separate defect scenarios in the simulations, as indicated above.

Weld formation simulations executed at Bay Zoltán Nonprofit Ltd. for Applied Research (BZN) produced local grain orientation over two grids, 0.25 and 2 mm. The latter is a widely accepted pragmatic choice sufficient for supporting inspections. Hence, the delay laws came from ray models over a 2 mm grid. The same 2 mm grid determined the orientation layout in time-domain FE simulations (numerical "experiments").

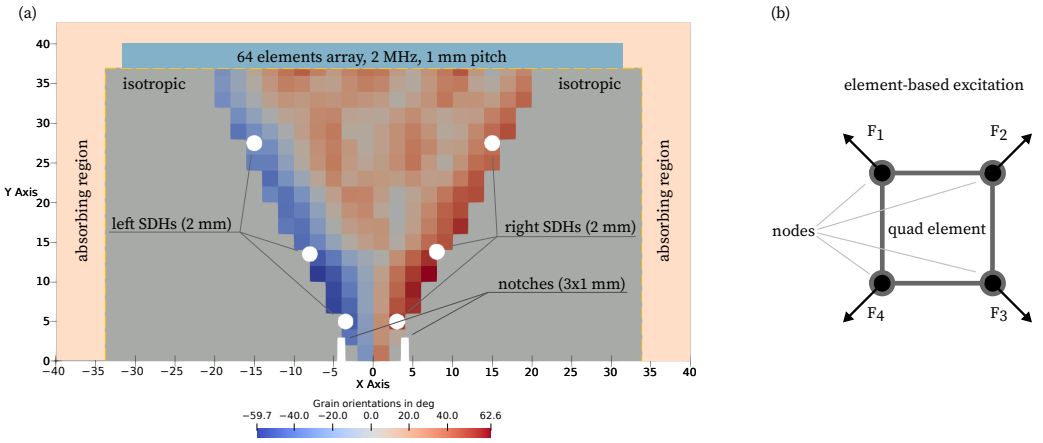

Figure 6. Schematic diagram of the ultrasound FE model setup with defect scenarios considered: (**a**) the model domain; (**b**) element excitation.

The domain shown in Figure 6 was meshed using regular quadrilateral elements (CPE4), with an element size of 0.04 mm, which gives more than seventy elements per longitudinal wavelength in the parent material. The time step was 6.21 ns, and simulation time ensured that all signals reflected from the backwall were comfortably captured. We modelled the ultrasonic array as a series of "element" excitations; that is, we applied a set of four equal forces acting outward from the element (see Figure 6). Assuming a 64-element array with a pitch of 1 mm and an element width of 0.7 mm, the exciting element was sought in the vicinity of the theoretical centre of each transducer. On reception, the out-of-plane response at a node closest to the theoretical centre of each transducer was recorded. The physical domain was surrounded by absorbing regions along all sides, except for the backwall, to minimise reflections and surface effects not considered in this study. Further, to better expose the effect of modified delay laws on defect signatures, for each considered case, we subtracted the results obtained for an "intact" structure from the structure with target defects.

4.2. Calculating Delay Laws with a Ray Model

Including material information in ultrasonic imaging requires calculating travel times between array elements and all points in the imaged domain. In this study, we used a shortest ray path model developed for the ADVISE project. The model is based on the Fermat principle, stating that the ultrasound takes the path which results in the shortest propagation time, analogously to previously reported implementations [30] above.

The present model uses a macroscale weld map description of the orientations. The edges of each square cell are seeded with a chosen number of nodes which helps to define an allowable number of paths the ultrasound can take while passing through each cell. The solver uses classical shortest path finding algorithms (here we use the `scipy` implementation) with local travel times across cells calculated from the group slowness of the rotated transversely isotropic material. A generic diagram behind this model (not limited to welds) is shown in Figure 7. Thanks to the cells having the same structure and using the same base group slowness for the weld and constant wavespeed for any isotropic material, the algorithm is quick for a large number of sources and target positions. The outputs of this calculation are the times of flight between all transducer positions and all points in the imaging grid.

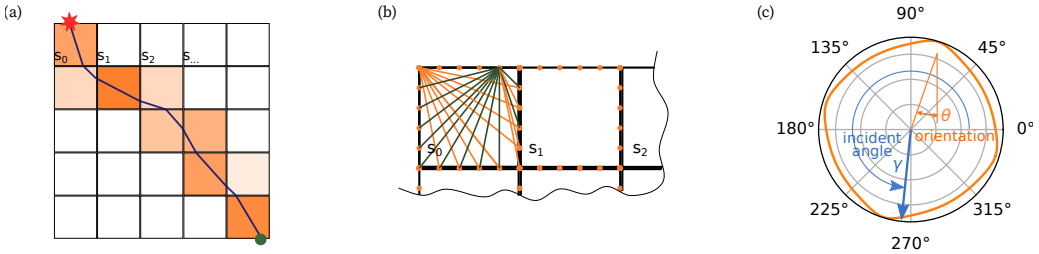

Figure 7. Schematic diagram of the shortest ray path model: (**a**) a discretised domain with an illustrative ray path; (**b**) magnified cells with edge seeding and allowable ray paths from two example seeds; (**c**) group slowness for a transversely isotropic material with grain orientation and an incident angles depicted.

5. Assessing the Impact of Welding Parameters on Ultrasonic Images

This section reports on the results of inspection simulations and the computation of ultrasonic images with supporting material information coming from different weld formation models. The assessment focuses on the cases and weld model parameters listed in Section 3.2.

5.1. Methodology

Finite element simulations included three defect scenarios, (a) SDHs along the left chamfer; (b) SDHs along the right chamfer; and (c) notches in the vicinity of the weld root. Each of these cases was considered in separate simulations. To compare the effect of weld model parameters, we used the SNR of each target defect. First, we calculated the SNRs for the "reference" case, described in Section 3.2. The values for each subsequent case were calculated in relation to that nominal value.

The SNR was calculated as follows, (i) the region of interest (ROI) was identified around the expected defect location; (ii) a maximum of the image was identified within the ROI; (iii) the ROI was repositioned, so that the maximum was at the centre and the value of the maximum was recorded as $I_{\max}$; (iv) the root mean square (RMS) of the image across the ROI, with the except of the "defect" area was recorded as noise; and (v) the SNR was calculated as:

$$\mathrm{SNR} = 20 \log_{10} \frac{|I|_{\max}}{|I|_{\text{noise, RMS}}} \tag{10}$$

The calculation is schematically depicted in Figure 8.

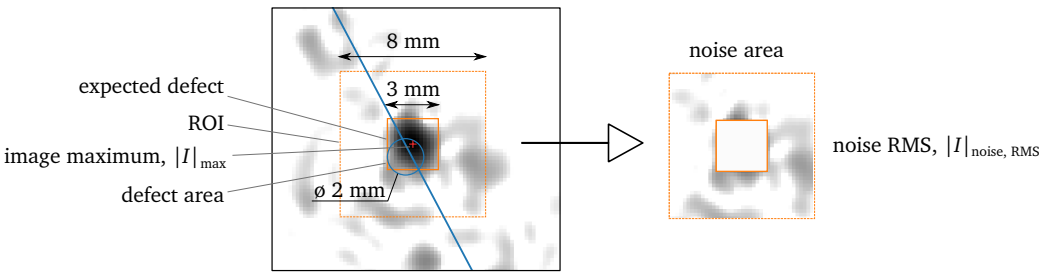

Figure 8. SNR calculation.

For the SDHs located close to the backwall, the ROI was slightly offset to avoid being affected by the backwall signature. For the same reason, for the notches scenario, the ROI and the defect area were rectangular (3×1 mm and 1×0.2 mm, respectively) enclosing the tip of the notch only, as we considered the tip to be the feature of interest. When presenting the impact of modified weld model parameters, we present the SNR in the "reference" setup and the change in the SNR as well as the shift in the image maximum.

5.2. The Impact of Material Information

First, we demonstrate the importance of accounting for heterogeneity in the imaging of the weld under consideration. Case 1 is compared to a dataset computed under the isotropic material assumption, which underpins the conventional approach to imaging. For the latter, the material in the weld region is assumed to be the same as the isotropic parent material for computing delay laws. In the FE inspection simulation, we used the "reference" orientation layout.

The results are shown in Figure 9. The images are scaled with respect to the maximum amplitude of either the middle SDH or one of the notch tips and the colour range is limited to −20 dB to aid visualisation. Isotropic delay laws degrade the SNR of all features notably, rendering some of them, e.g., the bottom right SDH and the notch tips illegible. The chosen weld configuration does not show significant beam deviation, and the defect signatures are misplaced by less than 2 mm at maximum. Figure 9 demonstrates how the isotropic delay laws spread the energy of the reflector spatially, contributing to elevated noise level and confirming that material information is an essential component of imaging in complex-structured materials.

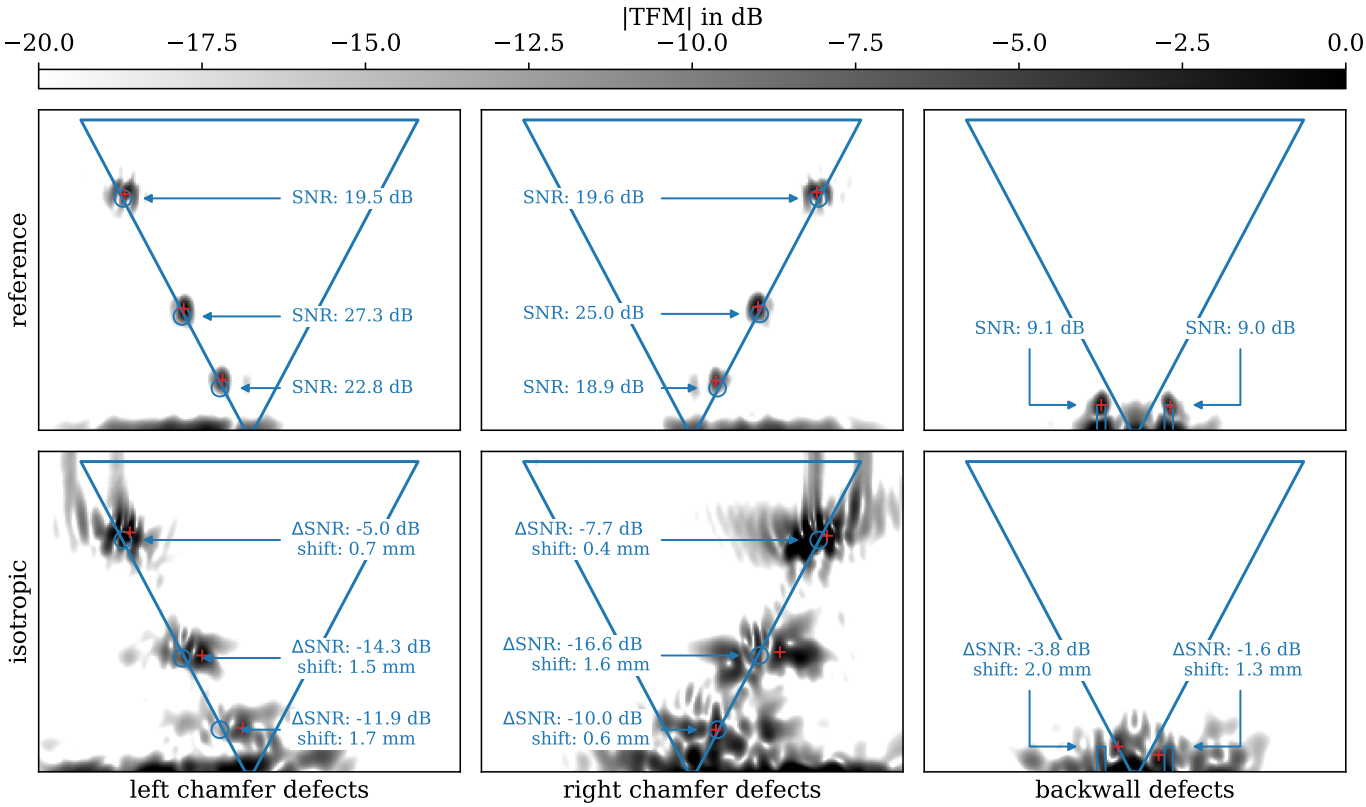

Figure 9. The effect of including material information in imaging—a comparison between the "correct" and isotropic delay laws.

5.3. Weld Path—Changing the Path Layout

Let us now consider the impact of the weld path layout. While the order of passes is usually carefully recorded, this comparison sheds light on the importance of this information for ultrasonic imaging. We compare Case 1 which had the right-to-left ordering with a simulation assuming the so-called American path layout (Case 2). In this configuration, the passes are placed on the chamfer first, with the last pass deposited in the middle. Figure 10 shows the orientation layout and the differences in local angles with reference to the "nominal" setup.

TFM images for this modification are presented in Figure 11. The shift of defect signatures is negligible. As in all cases, the defects furthest from the array are expected to

be more severely affected. This is also the case here—the right bottom SDH is the most severely affected, with the SNR reduction of more than 5 dB. We note that one weakness of this metric is that it takes the magnitude of a single pixel as the "signal" component and the average RMS across an area as "noise". For maxima that are spatially highly localised, the legibility may not be well represented. Given that the difference in local orientations is confined to a certain area of the weld, as Figure 10 suggests, the overall impact of the path layout modification is not very significant for most defects considered.

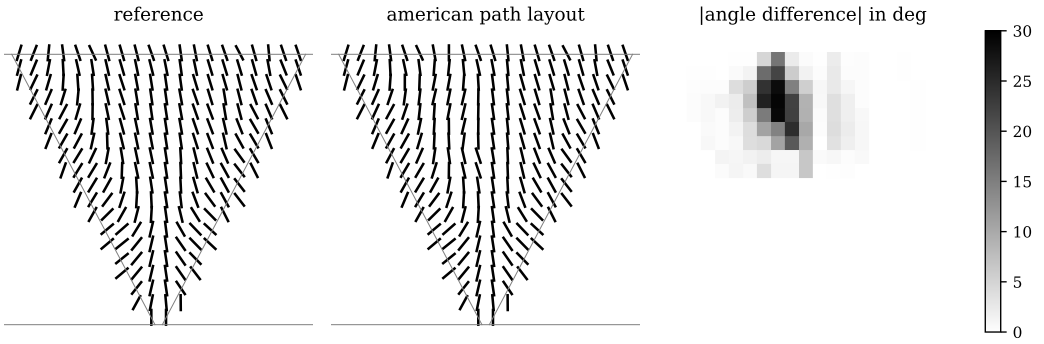

Figure 10. Local grain orientation for Case 1 and Case 2.

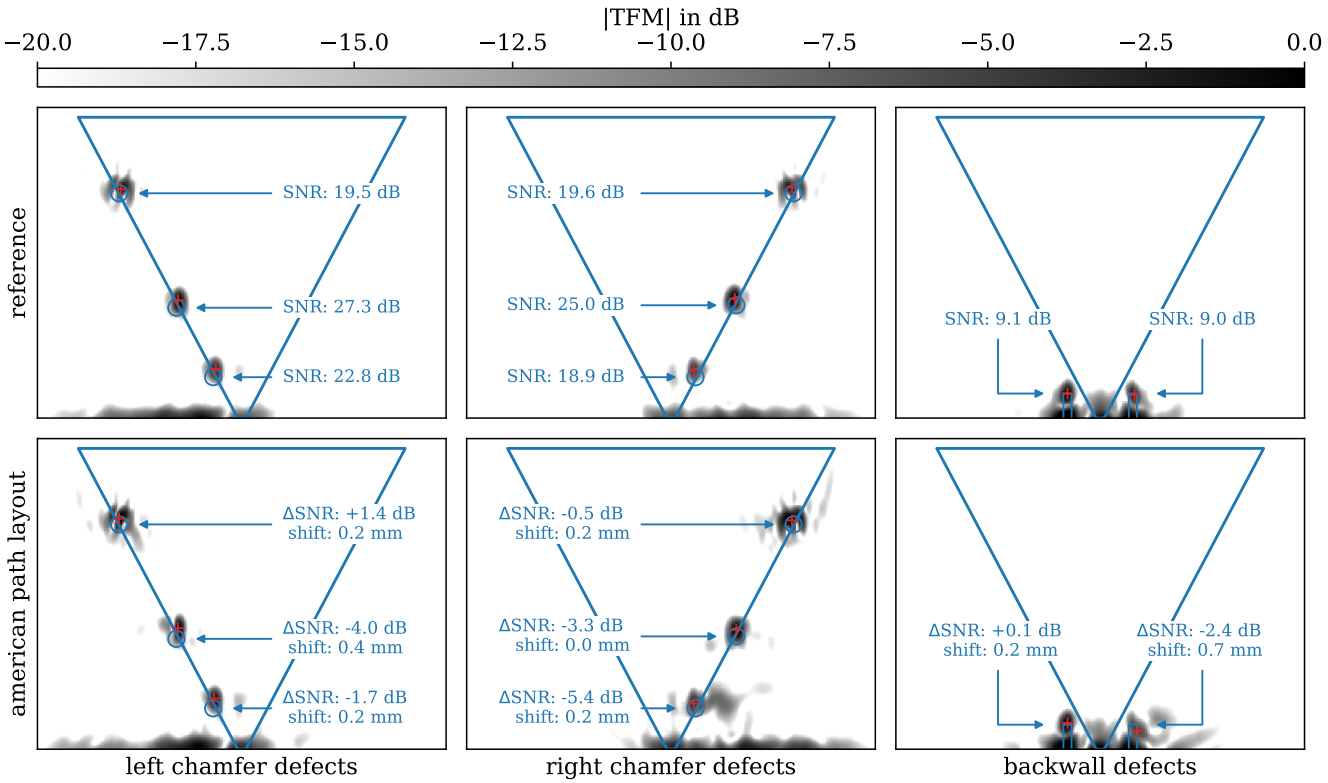

Figure 11. The effect of the modified weld path (the American layout of passes) on TFM images.

5.4. Electrode Tilt

This section considers electrode tilting. In practice, tilt is often present, but it is difficult to measure the angle or maintain a constant orientation during manual welding. In phenomenological modelling, electrode tilt is usually estimated or assumed within a reasonable range. We analysed two configurations here, (i) 8° tilt on all rows starting from the 4th (Case 3); and (ii) −5° tilt on all rows starting from the 4th (Case 4). The resulting grain orientations are shown in Figures 12 and 13, respectively.

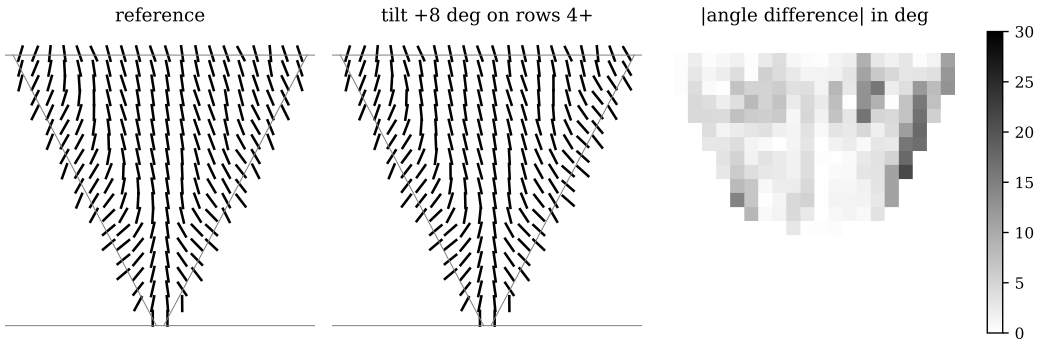

Figure 12. Local grain orientation for Case 1 and for Case 3 (with 8° tilt on all rows starting from the 4th).

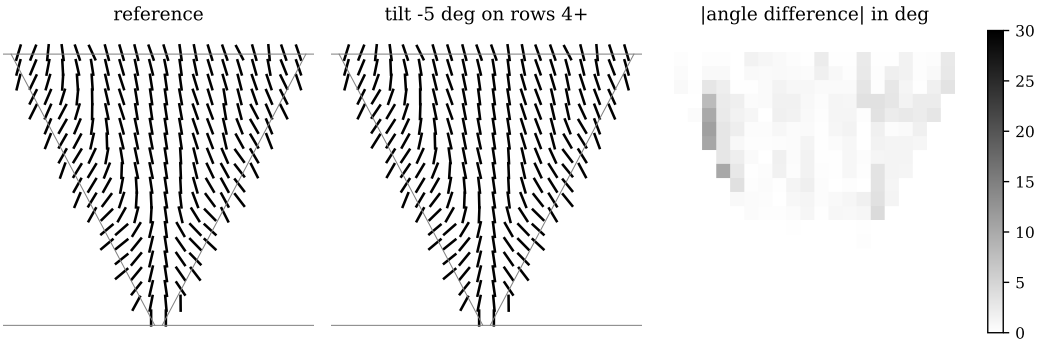

Figure 13. Local grain orientation for Case 1 and for Case 4 (with −5° tilt on all rows starting from the 4th).

Ultrasonic images computed for the two tilt angles are presented in Figures 14 and 15. The impact of accounting for the tilt is negligible, even though there are some differences in local angles across a large proportion of the weld. For the 8° tilt they are higher, but with their non-uniform distribution across the weld and the averaging function of the imaging procedure (many paths contribute to each pixel and each path is differently perturbed by the modification), the negative impact on the image is limited.

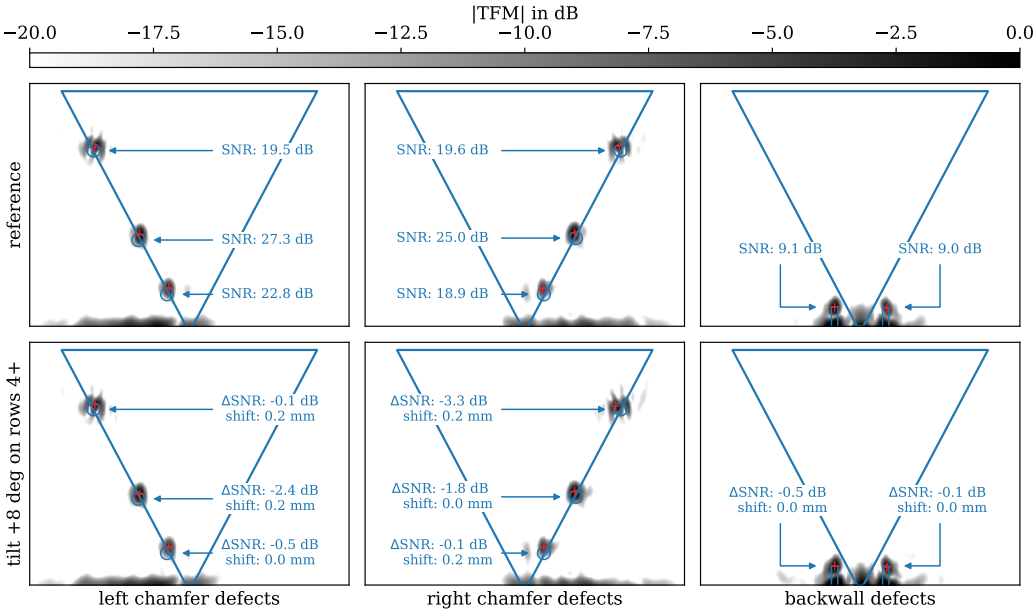

Figure 14. The effect of the electrode tilt (8° tilt on all rows starting from the 4th) on TFM images.

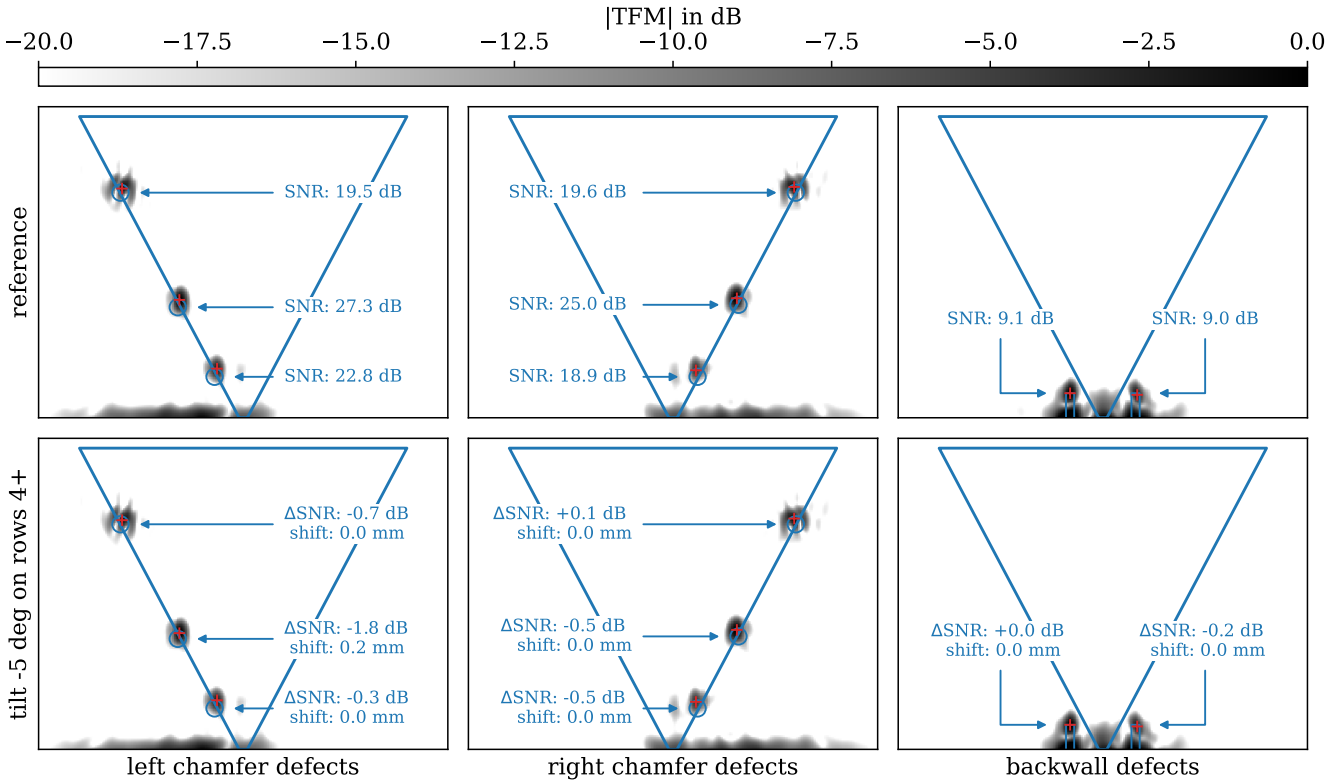

Figure 15. The effect of the electrode tilt (−5° tilt on all rows starting from the 4th) on TFM images.

5.5. Welding Power

We now look at the effect of welding power in solidification simulation. We used increased welding power, which means that the line energy grew by 10 % (Case 5). The associated grain orientations and TFM images are presented in Figures 16 and 17, respectively.

The small differences in local orientations do not cause any significant difference in the TFM images. The SNR for all the defect scenarios considered remained unaffected (differences within 2 dB are regarded as related to artefacts).

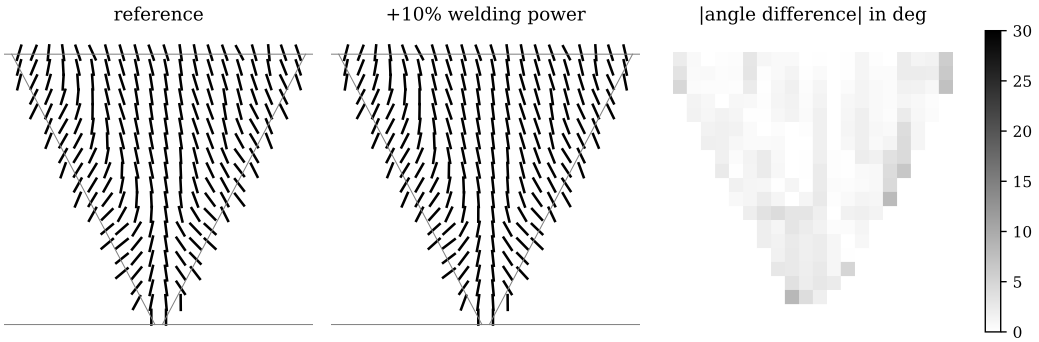

Figure 16. Local grain orientation for Case 1 and for Case 5 (with increased welding power).

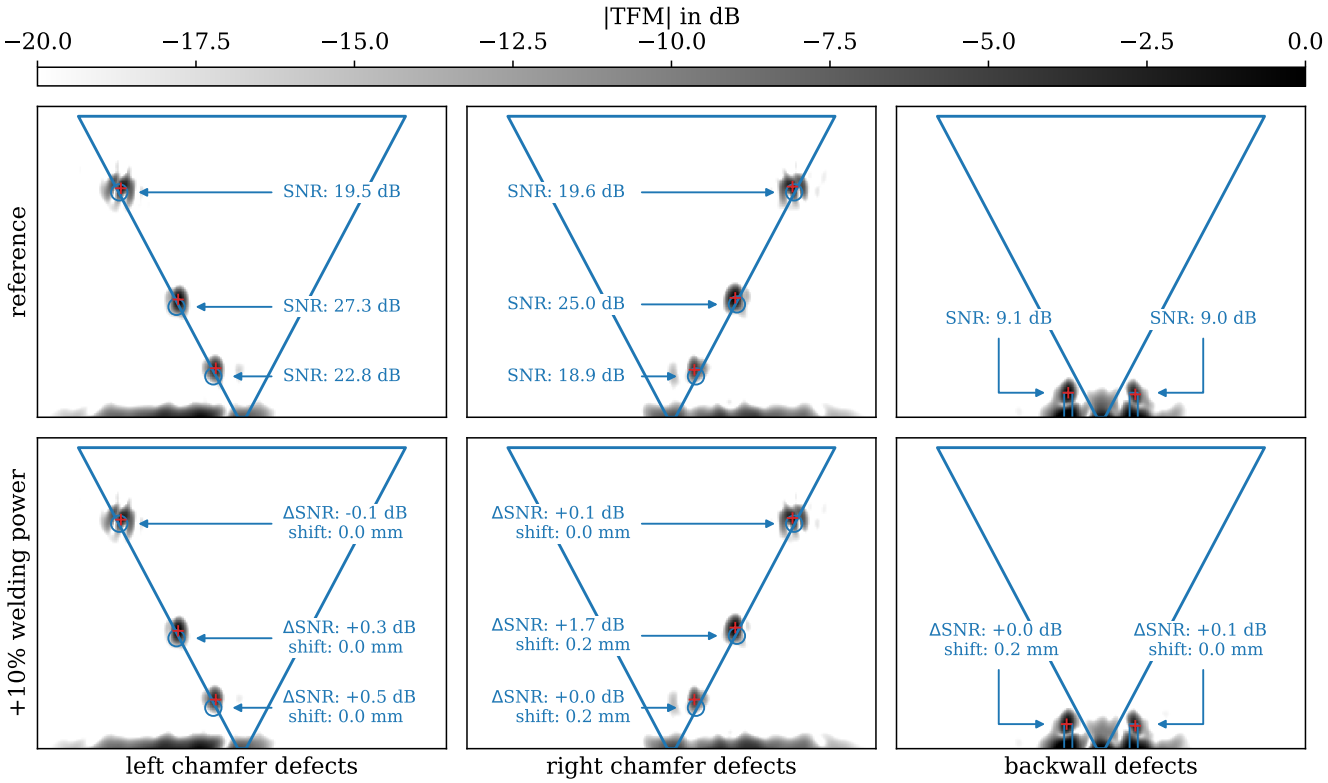

Figure 17. The effect of increased welding power on TFM images.

5.6. Weld Bead Shape

Both Case 1 and other models considered so far were built with an assumption of simplified, quadrilateral-shaped weld beads. This section illustrates the impact of considering more realistic geometries. The total bead area was determined based on the literature and the available welding parameters recorded during the manufacturing. After the third row, the weaving technique was considered. The resulting shapes were shown before, in Figure 5. We analysed three cases, (i) "nominal" beads (Case 6); (ii) smaller beads (half the size of the electrode), meaning larger heat input and deeper penetration of the heat source (Case 7); and (iii) large weaves—lower heat input and shallow penetration (Case 8). The resulting orientations are presented in Figures 18–20, respectively.

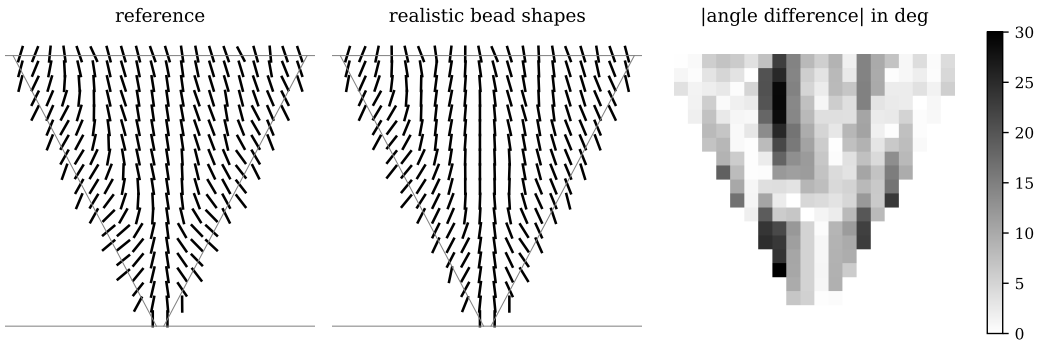

Figure 18. Local grain orientation for Case 1 and for Case 6 (with realistic, "nominal" weld bead geometry).

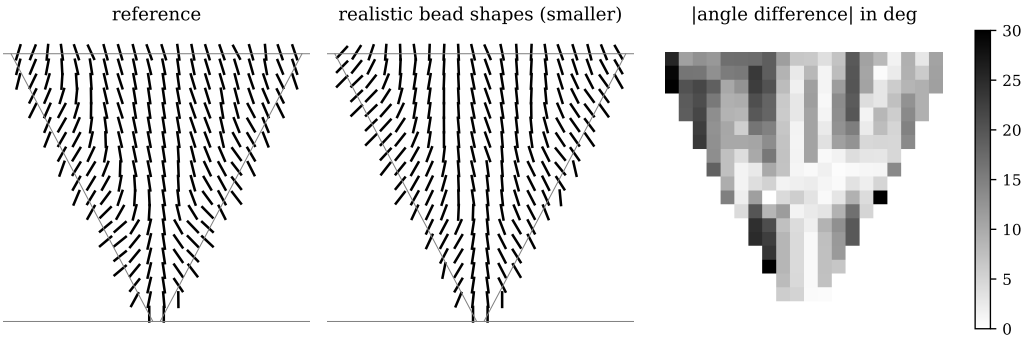

Figure 19. Local grain orientation for Case 1 and for Case 7 (with realistic, but smaller weld beads).

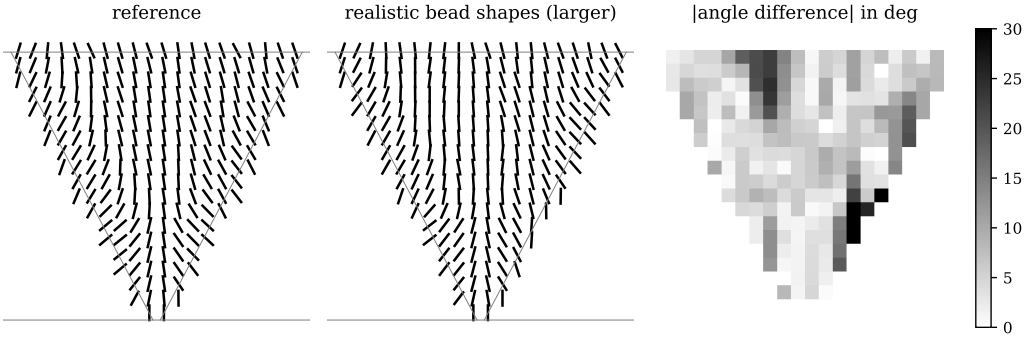

Figure 20. Local grain orientation for Case 1 and for Case 8 (with realistic, but larger weld beads).

TFM images for realistic bead geometries (nominal, smaller, and larger) are shown in Figures 21–23, respectively. The figures indicate that including the weaving technique in weld formation models can have a significant impact on resulting TFM images, especially on the defects along the right chamfer in this considered case. We see that smaller weaves have less impact, which is rather straightforward if we acknowledge that beads with smaller weaves are more similar to simplified quadrilateral shapes than those with larger ones. The key observation is that capturing the shapes of weld beads correctly in solidification simulations is important for supporting ultrasonic imaging and that its effect is more prominent if the beads are likely not to resemble regular, convex geometries.

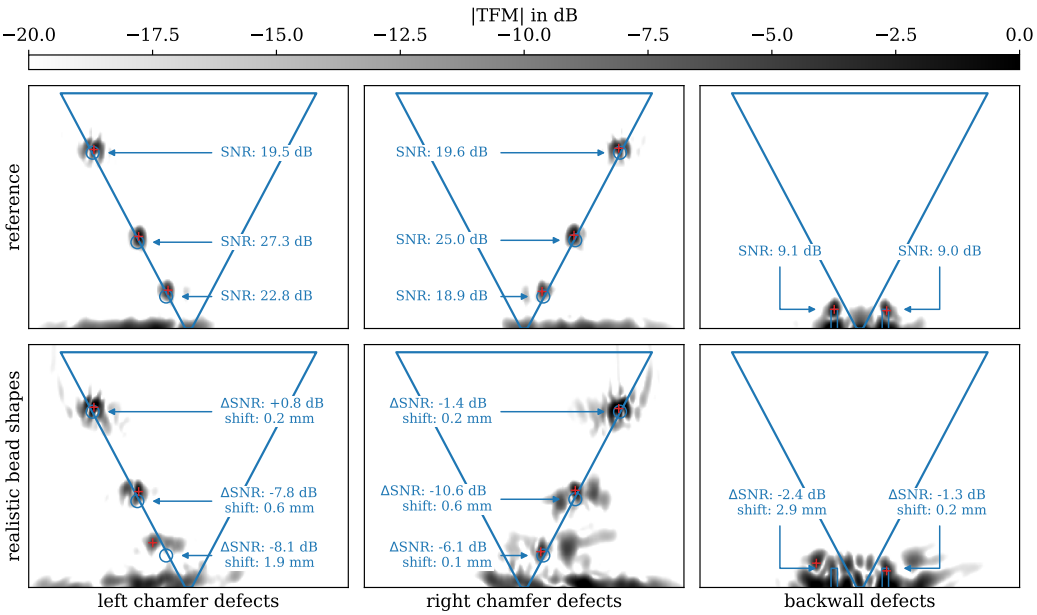

Figure 21. The effect of considering realistic weld bead geometry in the weld formation model (Case 6) on TFM images.

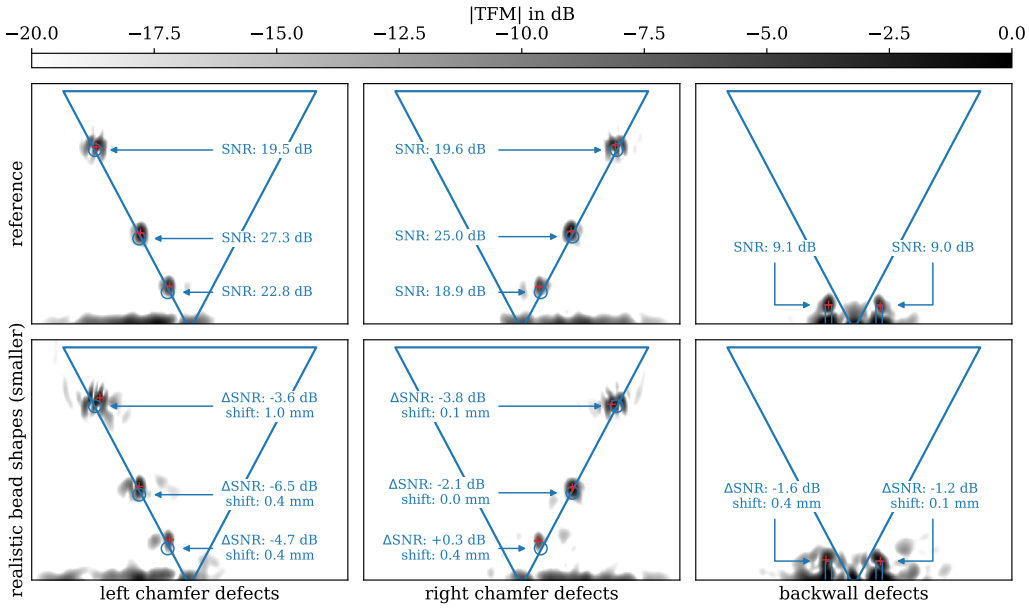

Figure 22. The effect of considering realistic weld bead geometry with smaller weaving in the weld formation model (Case 7) on TFM images.

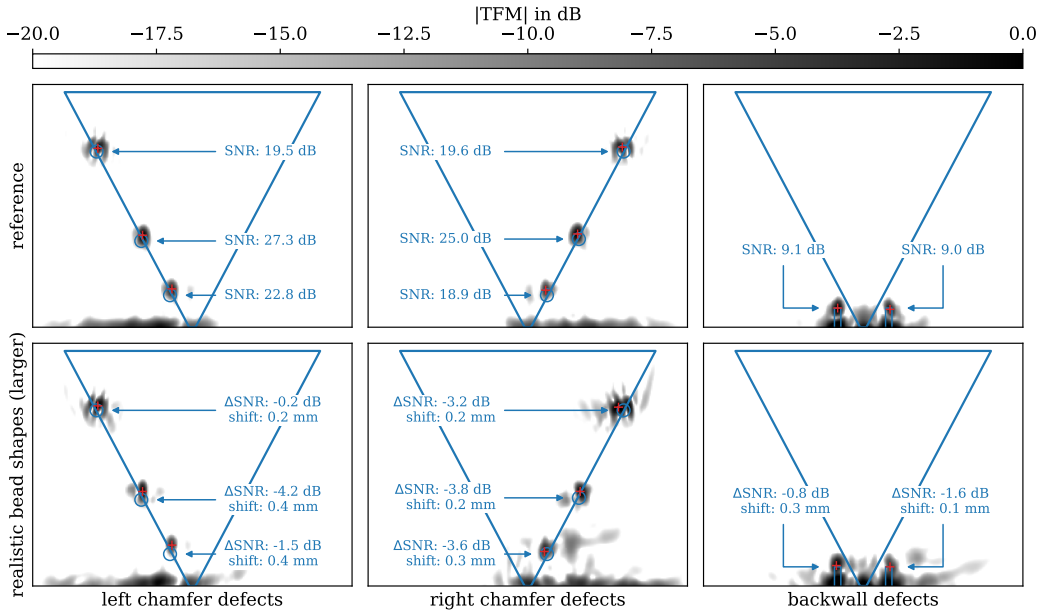

Figure 23. The effect of considering realistic weld bead geometry with large weaves in the weld formation model (Case 8) on TFM images.

Two further observations are worth mentioning. First, the images are scaled with respect to the maximum value in the ROI of middle SDHs. Consequently, in some cases, the "noise" part is in the lower part of the colour range. This may falsely suggest a better SNR, but, in reality, it may be associated with low defect amplitude as in the bottom right SDH in Figure 19. Second, the SNR calculation compares the local image maximum to area-averaged noise. The maximum may be an isolated pixel which would not appear prominent while visually assessing the image. While providing a useful quantitative metric, the established notion of the SNR is not ideal and does not fully represent the legibility of the defect signature.

5.7. 3D Effects—The Start and the Finish of the Arc

The NDE community agreed several decades ago that the effect of the out-of-plane grain orientation angle is small [13], and it is often ignored when modelling the propagation of ultrasound or simulating acquisitions. In this part, we performed a 3D weld formation simulation based on the simplified modelling paradigm. This allowed for analysing the effect of the out-of-plane grain tilt, but also the arc start and arc end effects which relate to the robustness of a weld map determined at a single location for the remaining part of a weld.

Figure 4c shows the FE mesh used in the weld formation model and the three locations along the weld axis used in the further comparison. While 3D simulations produces 3D orientations, we use a simplified approach in this paper, related to the common practice in the community, and use two angles for each cell—the angle in the plane of the cross-section, and the out-of-plane tilt along the weld axis. Let us first look at the resulting grain orientations predicted by the 3D model. The comparison focuses on the differences in angles read at the arc centre (Case 9) and those at arc extremities across both planes. First, Figures 24 and 25 show the angles over the plane of the cross-section for the arc start (Case 10) and arc finish (Case 11), respectively. They indicate no significant difference along the length of the weld, except for a few spot discrepancies. The out-of-plane grain angle tilt for the two locations is depicted in Figures 26 and 27. While the arc start shows approximately a constant angle difference against the arc centre across most of the weld (mainly in the range 5° to 15°), towards the end of the arc, the discrepancy tends to be more localised and slightly higher.

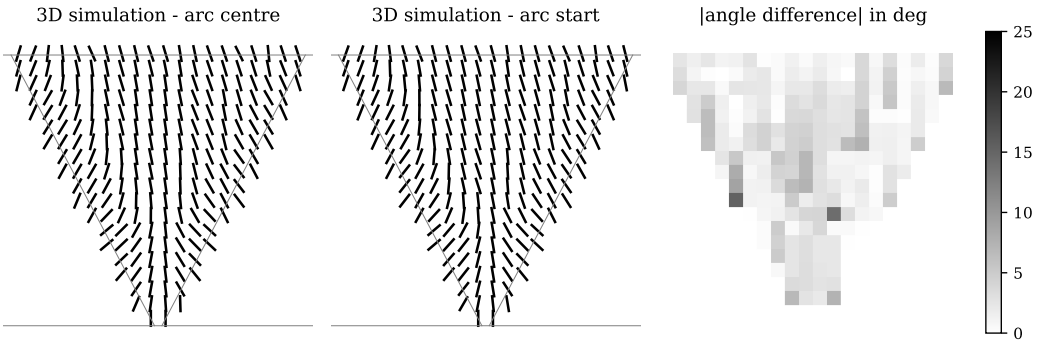

Figure 24. Local grain orientation across the plane of the cross-section computed by the 3D model—arc centre (Case 9) vs. arc start (Case 10) location.

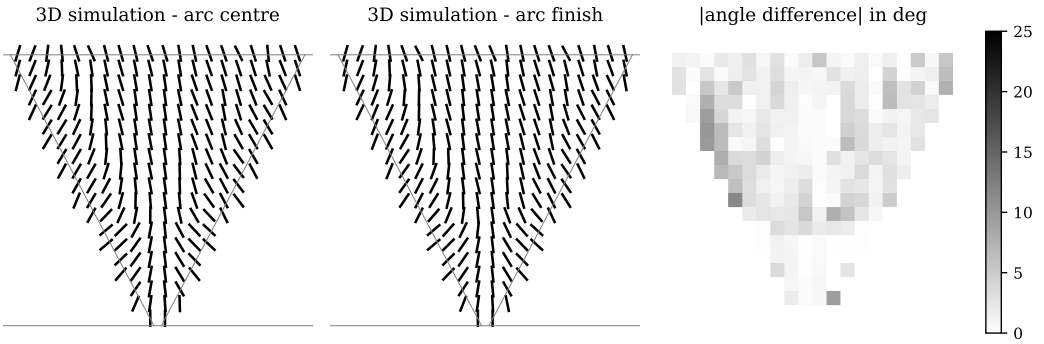

Figure 25. Local grain orientation across the plane of the cross-section computed by the 3D model—arc centre (Case 9) vs. arc finish (Case 11) location.

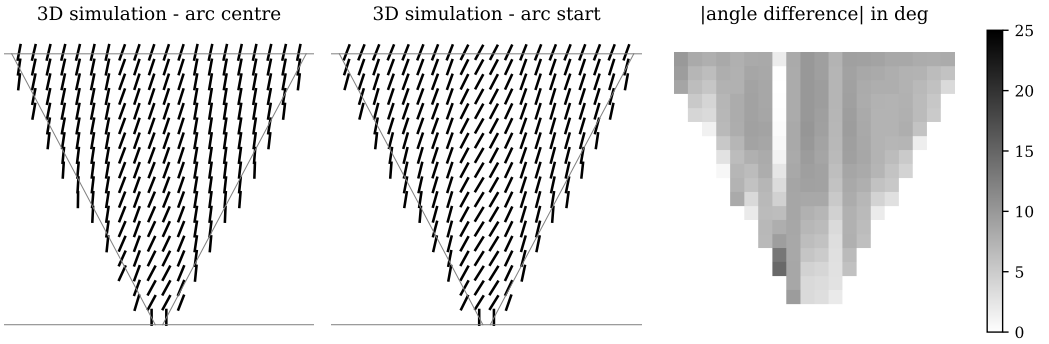

Figure 26. Out-of-plane tilt of the local grain orientation computed by the 3D model—arc centre (Case 9) vs. arc start (Case 10) location.

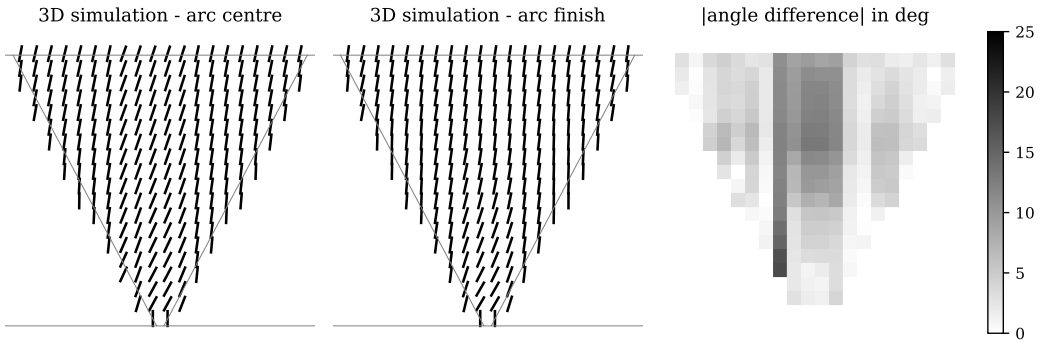

Figure 27. Out-of-plane tilt of the local grain orientation computed by the 3D model—arc centre (case 9) vs. arc finish (Case 11) location.

The FE simulations of ultrasonic acquisitions are in this case also in 2D, but 3D orientation angles are used to determine the local elastic tensor. Unlike in the previous cases, the "reference" image is now the image computed with delay laws based on the "arc centre" (Case 9) 3D orientations, including the out-of-plane component, analogous to the acquisition simulation. Figure 28 shows the images with the acquisition taken at the arc start location (Case 10). The top row of images acts as a reference. If we had only the 3D orientations computed at arc start, we would observe a decrease in the SNR of the defects increasing towards the backwall, as seen in the middle row. The notches are more severely affected—their signatures are not distinguishable any more. In the case when the TFM image was computed solely on the basis of the 2D delay laws from the simplified model used before in this paper, the defects close to the backwall and the right chamfer would not be legible any more.

We now consider acquisition at the arc centre location in Figure 29. First, the middle row shows the effect of neglecting the out-of-plane tilt when computing delay laws. The SNR reduction reaches over 15 dB at the bottom of the right chamfer, suggesting that the out-of-plane tilt may play a significant role. The 2D orientations from the simplified model used at the beginning of the paper perform comparably and show very similar SNR reduction. These results question the common practice of neglecting the out-of-plane grain tilt, indicating that including this information may enhance the legibility of signatures located further from the array.

Finally, the arc finish location (case 11) is addressed in Figure 30. While a small-to-moderate reduction in the SNR exists, all defect signatures retain their legibility, irrespective of the choice of the delay laws variant.

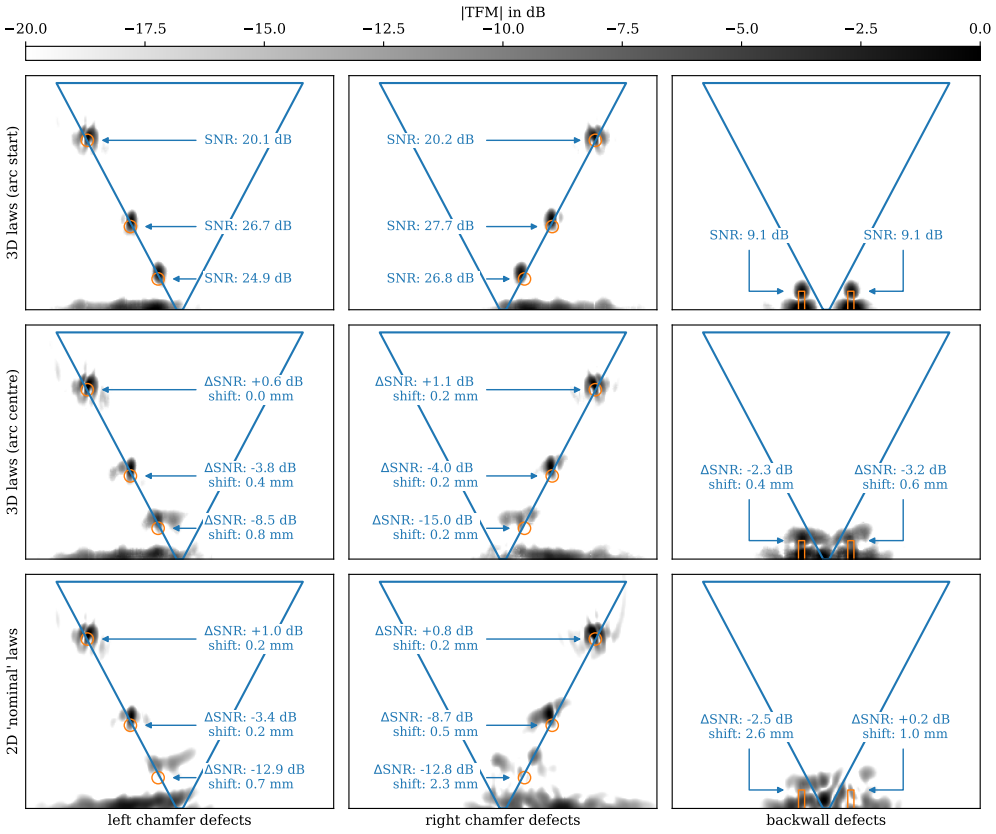

Figure 28. TFM image from the acquisition simulated at the arc start location based on 3D orientations from the 3D weld formation model.

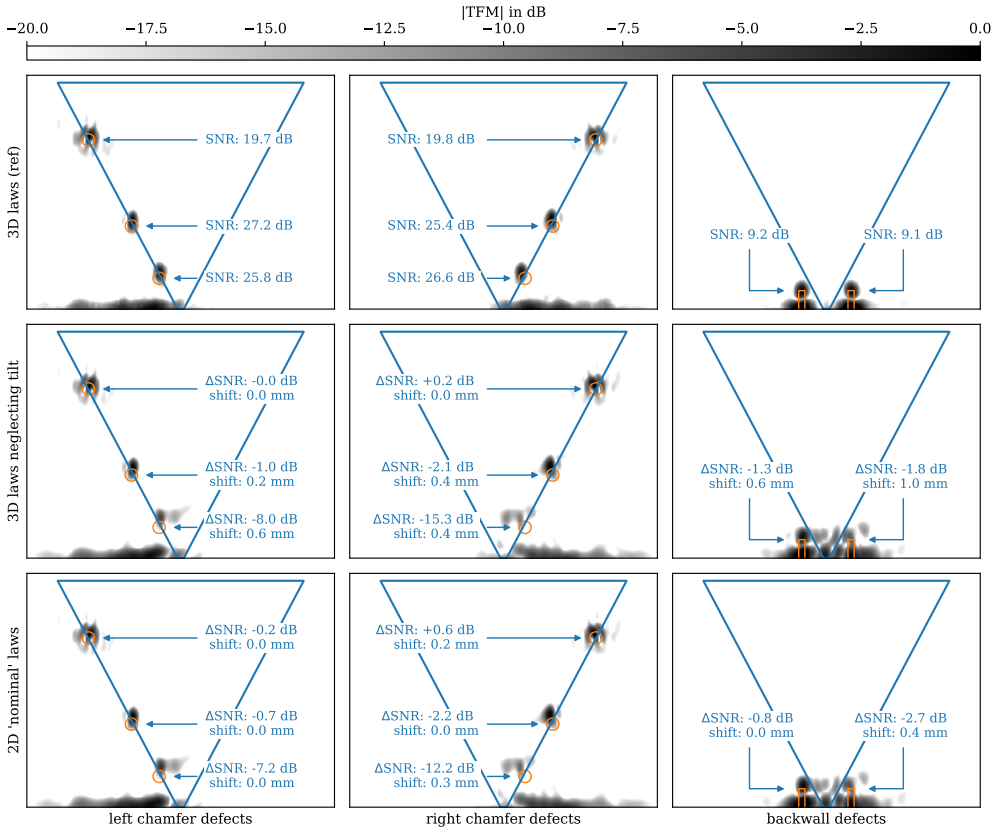

Figure 29. TFM image from the acquisition simulated at the arc centre location based on 3D orientations from the 3D weld formation model.

This section demonstrates that the 3D effects play a role in interpreting ultrasonic images, especially for defects located further away from the array, and close to the extremities of the joint in the welding direction (arc centre and arc finish). While the considered example questions the common practice, we note that the out-of-plane orientations were computed using the simplified FE weld formation model which has not, to date, been extensively scrutinised against fully coupled simulation. This is currently a topic of active research.

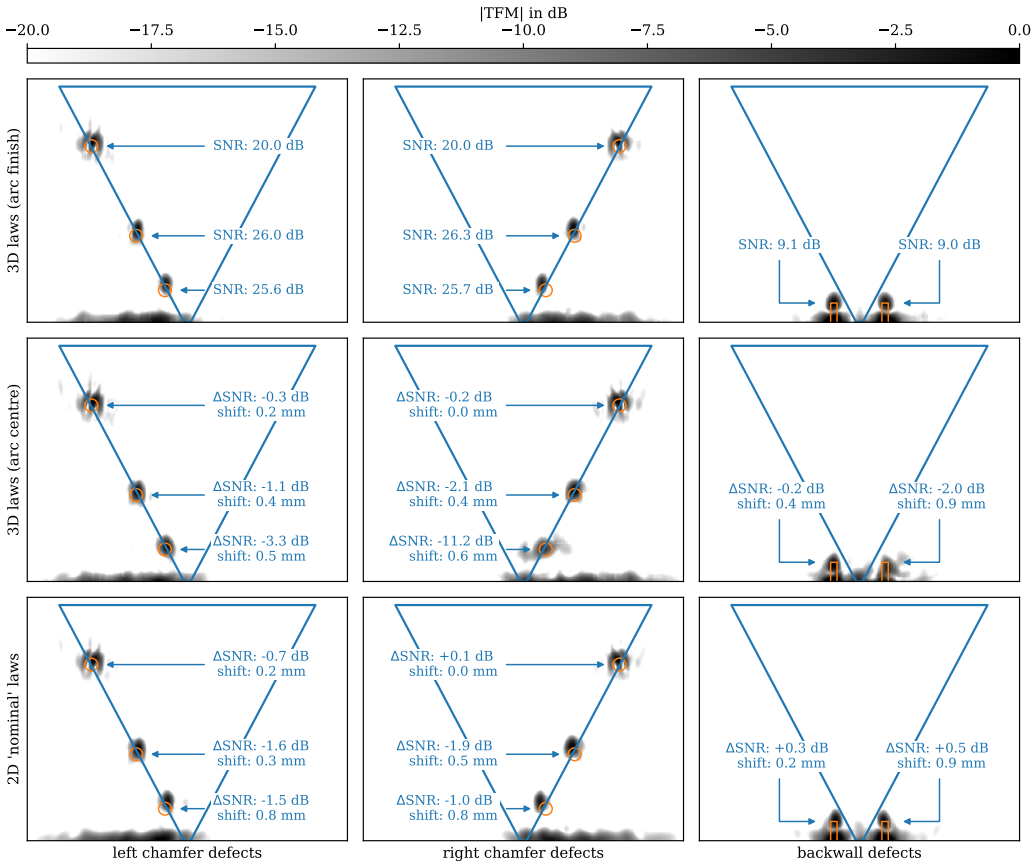

Figure 30. TFM image from the acquisition simulated at the arc finish location based on 3D orientations from the 3D weld formation model.

5.8. Mechanical Deformation

The final assessed feature of the weld formation model is the inclusion of mechanical deformation in solidification modelling. This effect is well agreed to be fundamental for simulations aimed at calculating, e.g., residual stress, but its importance for supporting ultrasonic imaging is still discussed in the community. With mechanical deformation, the weld formation model is considerably more complex, and it represents a coupled phenomenon. Hence, the solution is costly, and only a small number of 2D simulations can be performed in a reasonable time. The 3D model is too computationally demanding to be a viable option for supporting TFM imaging. In this context, the team at BZN proposed a pragmatic approach, where at the cost of ignoring the coupled effects, notable time gains are attained. The present comparison shows the impact of this assumption on TFM images.

Figure 31 depicts grain orientation comparison for the 2D thermal-only (Case 1) and coupled thermo-mechanical (Case 12) FE simulation. We observe notable differences, above 30°, both along the chamfer and in the upper left region of the weld. The coupled simulation produces a smoother map, visually more similar to the metallography image in Figure 2 than that coming from the thermal simulation only.

How this difference manifests itself in the TFM image is shown in Figure 32. The SNR for most defects is notably reduced by over 7 dB and the legibility of signatures decreased, especially for the SDHs close to the backwall and the notches (they rely on

longer propagation paths; hence, the delay law mismatch has a more prominent effect). The detrimental effect is moderate, indicating that neglecting mechanical deformation may be a promising pragmatic solution. While the SNR for most troublesome defects is reduced with the support of simplified thermal simulations, the CPU cost of the latter is notably decreased. Being a practically relevant factor, it contributes to the trade-off between solidification model complexity and the enhancement of TFM images.

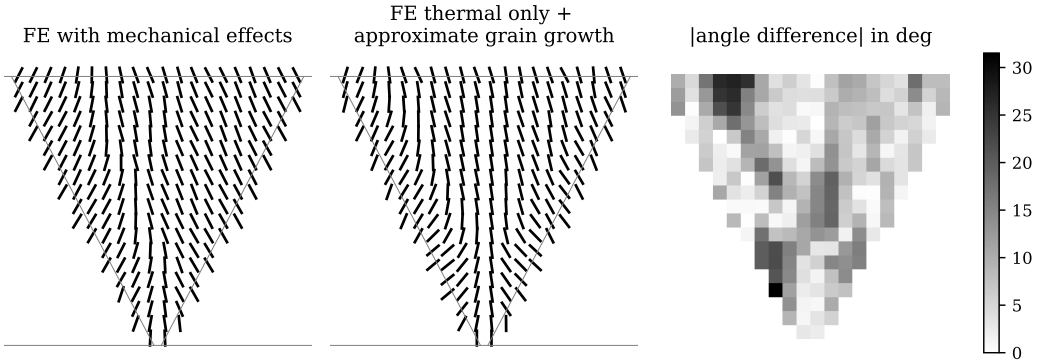

Figure 31. Local grain orientation for the coupled thermo-mechanical and solely thermal weld formation simulation.

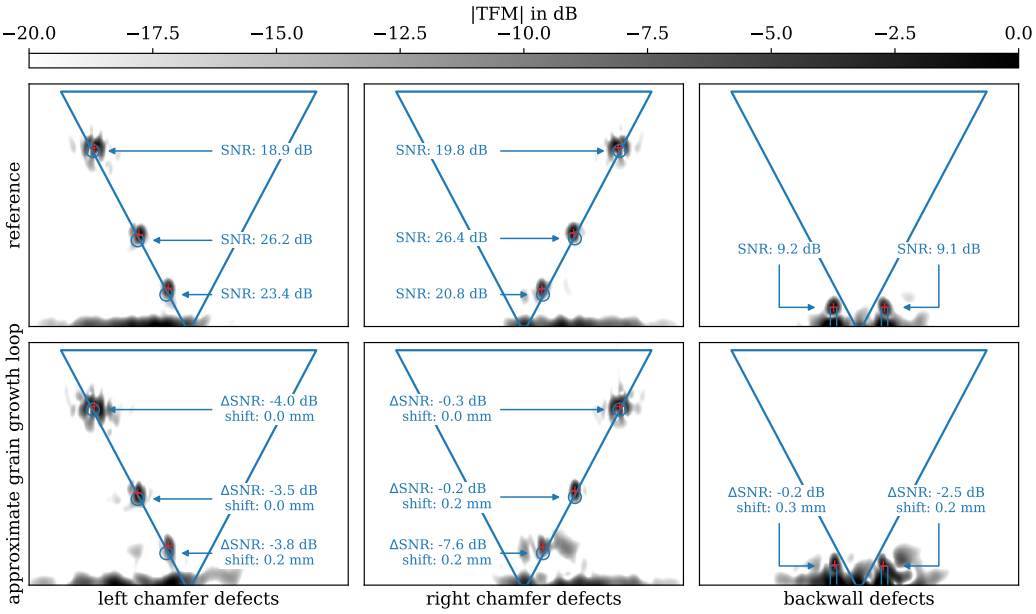

Figure 32. The effect of including mechanical deformation in weld formation simulation on the TFM imaging.

6. Verification on a Grain-Scale FE Model Based on the EBSD

This final section assesses the impact of including mechanical deformation in the solidification prediction on ultrasonic images once more—this time, simulating ultrasonic acquisition using a grain-scale FE model based on an EBSD measurement of the specimen. The EBSD measurement was performed at the University of Stuttgart.

The dataset recorded by the microscope was processed and reconstructed into a numerical microstructure using Dream.3D, a free software for polycrystal synthesis and reconstruction. The grains with their associated full 3D orientations were modelled in the FE model, solved by Pogo, with the same setup as described at the beginning of this paper. A schematic diagram of the FE model showing the grain structure is shown in Figure 33. For simplicity, the areas not covered by the weld were set to isotropic as in the model with macroscopic weld description. This time, we did not subtract the "background"

dataset from the signals with defects, which is expected to be a better representation of a realistic acquisition.

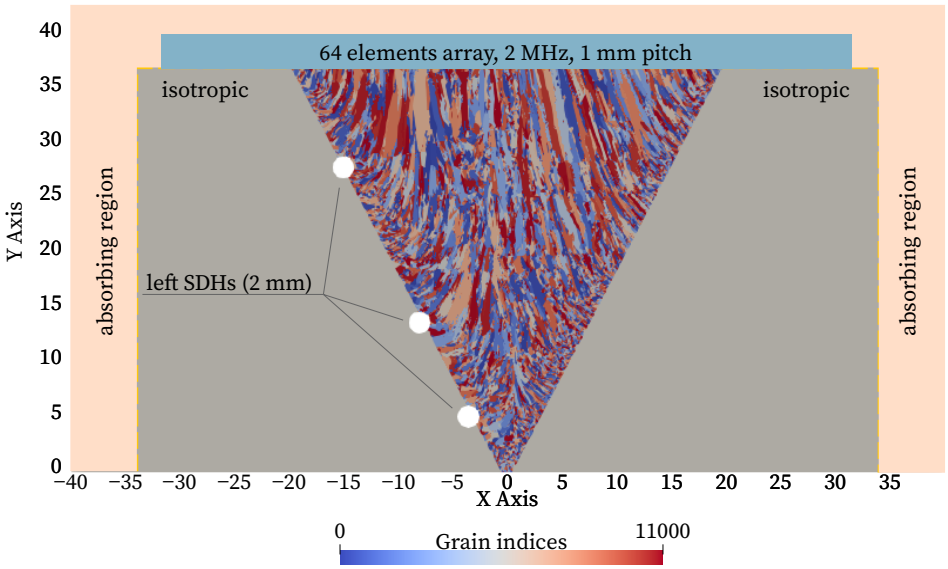

Figure 33. Schematic diagram of the EBSD-based FE model; only the left-chamfer defects are illustrated.

The TFM images for the defects along the left and the right chamfer are shown in Figures 34 and 35, respectively. We compare the effect of including the mechanical deformation in solidification simulations, a factor which was hypothesised to have less effect on ultrasonic imaging than it has on residual stress prediction at the beginning of this study. As in the previous examples, the images were scaled with respect to the magnitude at the middle SDH. To retain legibility, given the high level of grain noise, the magnitude range was limited to −12 dB from the maximum.

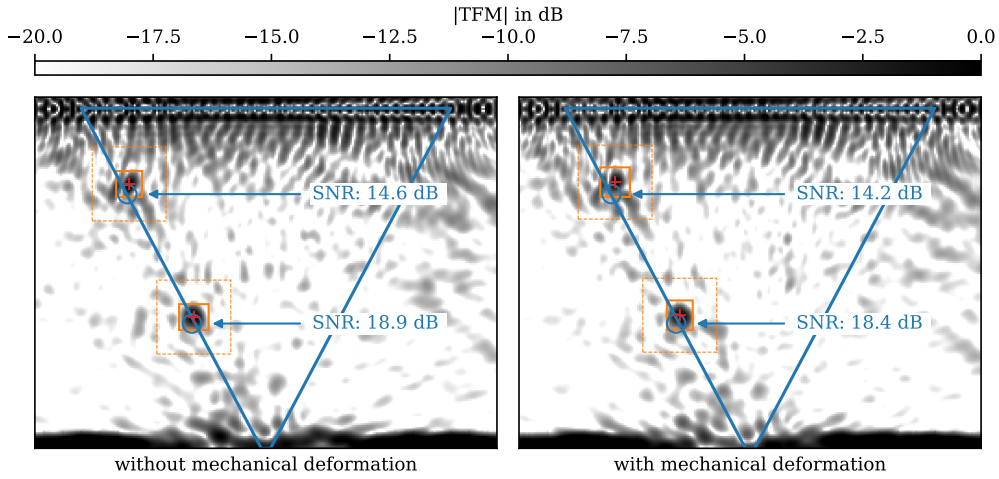

Figure 34. The effect of including mechanical deformation in weld formation simulation on the TFM images from time signals calculated using a grain-scale FE model based on the EBSD data (left chamfer defects).

The images based on the EBSD data show a significant level of noise, and not subtracting the "intact" datasets resulted in a strong influence of the array nearfield. Nevertheless, both the coupled thermo-mechanical simulations and the simplified approach presented a similar performance for the EBSD-based grain-scale numerical "experiment". For the case with defects on the left chamfer, defect SNRs are similar, but the one closest to the backwall could not be distinguished from the background noise.

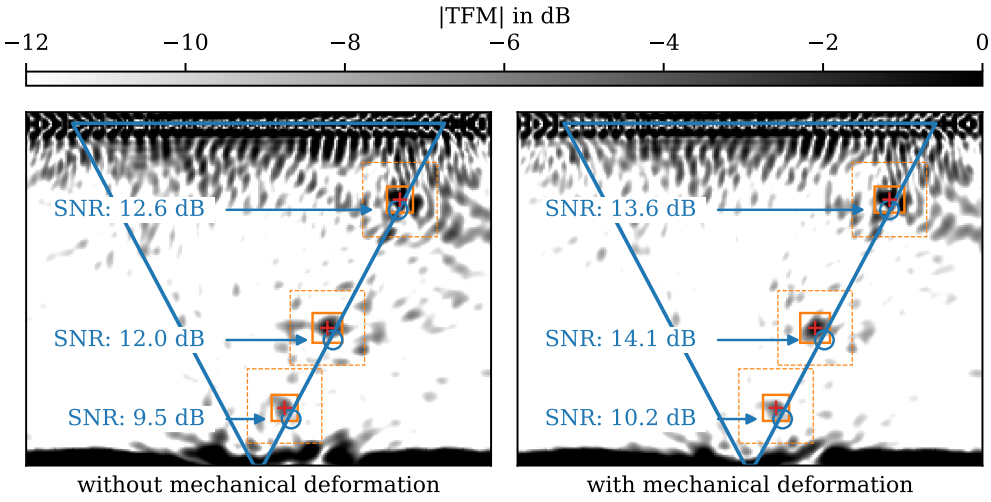

Figure 35. The effect of including mechanical deformation in weld formation simulation on the TFM images from time signals calculated using a grain-scale FE model based on the EBSD data (right chamfer defects.

For the imaging defects on the right chamfer, the level of noise is elevated, but all defects can be distinguished. A plausible explanation of the poorer performance for left-chamfer defects is that the EBSD scan was notably noisier over that area yielding results with a low confidence index. Consequently, the microstructure underpinning the FE ultrasound simulations could be not well represented by the solidification modelling. We should also mention that there are numerous factors at play in this example, which are impossible to account for, even for a numerical exercise. However, given that in reality many parameters are not known, this case is a good representation of a practical scenario.

7. Practical Implications

We tested several parameters used in weld formation modelling to learn about their significance in simulations aimed at supporting ultrasonic imaging of austenitic welds. While a single case study provides only a glimpse into the problem and is insufficient for drawing robust, quantitative measures, it allows for formulating general observations which we believe are useful for the community and set directions for future research in this area. In Table 7, we summarise the configurations tested using a simple "important/not important" classification.

Table 7. The significance of weld formation model parameters on TFM images calculated based on model-derived delay laws.

Feature	Importance
weld path	moderate
electrode tilt	low
welding power	low
bead shape	high
3D effects	moderate–high (arc start)
mechanical deformation	low–moderate (close to the backwall)

More importantly, the assumption taken at the beginning of this study allowing for neglecting mechanical deformation in solidification simulations for supporting ultrasonic imaging may be a pragmatic way towards employing physics-based solidification simulations to support ultrasonic imaging. The incentive of easy setup and execution of the thermal simulations with a potential of high-throughput calculation balances the moderate-to-low sacrifice in accuracy. Moreover, the results coming from simplified orientation calculations could be used in inversion methods based on ultrasound as starting points

for optimisation. The inversions are often ill-posed, meaning that the multitude of local minima is a significant challenge. Including a credible starting point would help to achieve convergence and to converge at the correct grain orientation configurations.

8. Conclusions

This paper reports a study investigating weld formation modelling as a support tool for ultrasonic imaging of austenitic welds. The local grain orientations predicted by such models can be used to calculate delay laws for ultrasonic imaging, enabling material information to be accounted for. Based on an existing mock-up manufactured for the ADVISE project, we developed a series of solidification finite element models to test the impact of model parameters on the legibility of a few chosen defect scenarios. Ultrasonic acquisitions were modelled in explicit finite element models so that full control of the properties of the structure is retained. This allowed us to focus the comparison solely on the effect of weld model parameters. The study identified the most critical parameters and investigated the significance of mechanical deformation during welding in predicting orientations for supporting ultrasonic imaging. The considered example suggests that expensive, fully coupled welding simulations may not be necessary to deliver orientation maps sufficient for ultrasonic imaging. This observation is promising for the NDE community, prompting further research into coupling FE thermal simulations with simplified grain growth representations.

Author Contributions: Conceptualization, M.K.K., M.J.S.L., A.S., Z.B. and S.S.; methodology, M.K.K., M.J.S.L. and Z.B.; software, M.K.K., Z.B. and B.S.; validation, M.K.K., Z.B. and B.S.; formal analysis, M.K.K., M.J.S.L., Z.B., B.S., S.S. and A.S.; investigation, M.K.K., Z.B. and B.S.; resources, M.J.S.L., A.S. and S.S.; data curation, M.K.K., Z.B. and B.S.; writing—original draft preparation, M.K.K., B.S. and Z.B.; writing—review and editing, M.J.S.L., S.S. and A.S.; visualization, M.K.K., Z.B. and B.S.; supervision, M.J.S.L., A.S. and S.S.; project administration, A.S.; funding acquisition, A.S., M.J.S.L. and S.S. All authors have read and agreed to the published version of the manuscript.

Funding: This work is supported by the ADVISE project (www.advise-h2020.eu accessed on 10 July 2023) funded by the Euratom research and training programme 2014–2018 under grant agreement no. 755500.

Institutional Review Board Statement: Not applicable.

Informed Consent Statement: Not applicable.

Data Availability Statement: Not applicable.

Acknowledgments: The authors thank partners from the ADVISE project, especially the University of Stuttgart and Fabian Schreyer for providing the sample and EBSD data.

Conflicts of Interest: The authors declare no conflict of interest.

References

1. Holmes, C.; Drinkwater, B.W.; Wilcox, P.D. Post-Processing of the Full Matrix of Ultrasonic Transmit–Receive Array Data for Non-Destructive Evaluation. *NDT E Int.* **2005**, *38*, 701–711. [CrossRef]
2. Hunter, A.J.; Drinkwater, B.W.; Zhang, J.; Wilcox, P.D.; Thompson, D.O.; Chimenti, D.E. A Study into the Effects of an Austenitic Weld on Ultrasonic Array Imaging Performance. In *Review of Progress in Quantitative Nondestructive Evaluation*; American Institute of Physics: College Park, MD, USA, 2010; Volume 30, pp. 1063–1070. [CrossRef]
3. Connolly, G.D. Modelling of the Propagation of Ultrasound through Austenitic Steel Welds. Ph.D. Thesis, Department of Mechanical Engineering, Imperial College London, London, UK, 2009.
4. Chassignole, B.; El Guerjouma, R.; Ploix, M.A.; Fouquet, T. Ultrasonic and Structural Characterization of Anisotropic Austenitic Stainless Steel Welds: Towards a Higher Reliability in Ultrasonic Non-Destructive Testing. *NDT E Int.* **2010**, *43*, 273–282. [CrossRef]
5. Connolly, G.D.; Lowe, M.J.S.; Temple, J.A.G.; Rokhlin, S.I. Correction of Ultrasonic Array Images to Improve Reflector Sizing and Location in Inhomogeneous Materials Using a Ray-Tracing Model. *J. Acoust. Soc. Am.* **2010**, *127*, 2802–2812. [CrossRef]
6. Ménard, C.; Robert, S.; Miorelli, R.; Lesselier, D. Optimization Algorithms for Ultrasonic Array Imaging in Homogeneous Anisotropic Steel Components with Unknown Properties. *NDT E Int.* **2020**, *116*, 102327. [CrossRef]

7. Ménard, C.; Robert, S.; Lesselier, D. Ultrasonic Array Imaging of Nuclear Austenitic V-Shape Welds with Inhomogeneous and Unknown Anisotropic Properties. *Appl. Sci.* **2021**, *11*, 6505. [CrossRef]
8. Kalkowski, M.; Lowe, M.; Samaitis, V.; Schreyer, F.; Robert, S. Weld Map Tomography for Determining Local Grain Orientations from Ultrasound. *Proc. R. Soc. A* 2023, *under review*.
9. Moysan, J.; Apfel, A.; Corneloup, G.; Chassignole, B. Modelling the Grain Orientation of Austenitic Stainless Steel Multipass Welds to Improve Ultrasonic Assessment of Structural Integrity. *Int. J. Press. Vessel. Pip.* **2003**, *80*, 77–85. [CrossRef]
10. Gueudre, C.; Le Marrec, L.; Moysan, J.; Chassignole, B. Direct Model Optimisation for Data Inversion. Application to Ultrasonic Characterisation of Heterogeneous Welds. *NDT E Int.* **2009**, *42*, 47–55. [CrossRef]
11. Langenberg, K.J.; Hannemann, R.; Kaczorowski, T.; Marklein, R.; Koehler, B.; Schurig, C.; Walte, F. Application of Modeling Techniques for Ultrasonic Austenitic Weld Inspection. *NDT E Int.* **2000**, *33*, 465–480. [CrossRef]
12. Spies, M.; Kröning, M. Ultrasonic Inspection of Inhomogeneous Welds Simulated by Gaussian Beam Superposition. In *Review of Progress in Quantitative Nondestructive Evaluation*; Springer: Boston, MA, USA, 1999; pp. 1107–1113. [CrossRef]
13. Ogilvy, J.A. Computerized Ultrasonic Ray Tracing in Austenitic Steel. *NDT E Int.* **1985**, *18*, 67–77. [CrossRef]
14. Koseki, T.; Inoue, H.; Fukuda, Y.; Nogami, A. Numerical simulation of equiaxed grain formation in weld solidification. *Sci. Technol. Adv. Mater.* **2003**, *4*, 183–195. [CrossRef]
15. Takaki, T.; Fukuoka, T.; Tomita, Y. Phase-field simulation during directional solidification of a binary alloy using adaptive finite element method. *J. Cryst. Growth* **2005**, *283*, 263–278. [CrossRef]
16. Duggan, G.; Tong, M.; Browne, D.J. An integrated meso-scale numerical model of melting and solidification in laser welding. *IOP Conf. Ser. Mater. Sci. Eng.* **2012**, *27*, 012077. [CrossRef]
17. Poole, W.J.; Militzer, M.; Garcin, T. An Integrated Model to Predict Microstructure and Mechanical Properties in the Heat Affected Zone for X80 Linepipe. In Proceedings of the 9th International Pipeline Conference, Calgary, AB, Canada, 24–28 September 2012.
18. Toloui, M.; Militzer, M. Phase Field Modelling of Microstructure Evolution in the HAZ of X80 Linepipe Steel. In Proceedings of the 2012 9th International Pipeline Conference, Calgary, AB, Canada, 24–28 September 2012; Volume 3: Materials and Joining.
19. Szávai, S.; Bézi, Z.; Dudra, J.; Méhész, I. Modelling of Phased Array Ultrasonic Inspection of a Steam Generator Dissimilar Metal Weld. In Proceedings of the 21st European Conference on Fracture (ECF21), Catania, Italy, 20–24 June 2016; Volume 2, pp. 1015–1022. [CrossRef]
20. Szávai, S.; Bezi, Z.; Ohms, C. Numerical simulation of dissimilar metal welding and its verification for determination of residual stresses. *Frat. Integr. Strutt.* **2016**, *10*, 36–45. [CrossRef]
21. Spisák, B.; Bézi, Z.; Szávai, S. Study of the Stress State of a Dissimilar Metal Weld Due to Manufacturing and Operational Conditions. *Period. Polytech. Mech. Eng.* **2022**, *66*, 120–128. [CrossRef]
22. Olson, D.L.; Siewert, T.A.; Liu, S.; Edwards, G.R. *Welding, Brazing, and Soldering*; ASM International: Almere, The Netherlands, 1993. [CrossRef]
23. Bouchard, P. Validated residual stress profiles for fracture assessments of stainless steel pipe girth welds. *Int. J. Press. Vessel. Pip.* **2007**, *84*, 195–222. [CrossRef]
24. Goldak, J.; Chakravarti, A.; Bibby, M. A new finite element model for welding heat sources. *Metall. Trans. B* **1984**, *15*, 299–305. [CrossRef]
25. Marmonier, M.; Robert, S.; Laurent, J.; Prada, C. Real-Time 3D Imaging with Fourier-domain Algorithms and Matrix Arrays Applied to Non-Destructive Testing. *Ultrasonics* **2022**, *124*, 106708. [CrossRef]
26. Alleyne, D.N.; Lowe, M.J.S.; Cawley, P. The Reflection of Guided Waves From Circumferential Notches in Pipes. *J. Appl. Mech.* **1998**, *65*, 635–641. [CrossRef]
27. Huthwaite, P. Accelerated Finite Element Elastodynamic Simulations Using the GPU. *J. Comput. Phys.* **2014**, *257*, 687–707. [CrossRef]
28. Van Pamel, A.; Sha, G.; Rokhlin, S.I.; Lowe, M.J.S. Finite-Element Modelling of Elastic Wave Propagation and Scattering within Heterogeneous Media. *Proc. R. Soc. A* **2017**, *473*, 20160738. [CrossRef]
29. Huang, M.; Sha, G.; Huthwaite, P.; Rokhlin, S.I.; Lowe, M.J.S. Maximizing the Accuracy of Finite Element Simulation of Elastic Wave Propagation in Polycrystals. *J. Acoust. Soc. Am.* **2020**, *148*, 1890–1910. [CrossRef]
30. Nowers, O.; Duxbury, D.J.; Zhang, J.; Drinkwater, B.W. Novel Ray-Tracing Algorithms in NDE: Application of Dijkstra and A* Algorithms to the Inspection of an Anisotropic Weld. *NDT E Int.* **2014**, *61*, 58–66. [CrossRef]